remote sensing

MDPI

Article

Sentinel-1 SAR Monitoring of River Water Surface Elevation: Effects of Wind, Waves, River Morphology and Vegetation

Feifei Pan

Department of Geography and the Environment, University of North Texas, Denton, TX 76203, USA; feifei.pan@unt.edu

Highlights

What are the main findings?

- Sentinel-1 SAR-derived river inundation areas (RIAs) and a topobathymetric elevation model (TEM)-based RIA–water surface elevation (WSE) relationship enabled river WSE estimation, with $\log_{10}$(VV) performing best overall.
- WSE errors were smallest at low flow, largest at medium–high flow, and decreased during flooding.
- Under medium–high flow, calm conditions generally produced smaller errors than non-calm conditions, with additional differences among wind orientations.

What are the implications of the main findings?

- Incorporating submerged channel bathymetry is important for constructing RIA–WSE relationships that can resolve low-stage WSE variations.
- SAR-estimated WSE accuracy reflects the combined effects of vegetation, wind-generated water surface roughness, and river morphology, rather than the influence of wind speed alone.
- SAR-derived WSE estimation accuracy varies substantially among flow regimes, highlighting the importance of flow-specific accuracy assessment.

Abstract

Accurate monitoring of river water surface elevation (WSE) is important for hydrologic and flood applications, particularly where in situ observations are limited. This study evaluates Sentinel-1 Synthetic Aperture Radar (SAR) for estimating river WSE using a river inundation area–water surface elevation (RIA–WSE) relationship derived from high-resolution topobathymetric elevation data and investigates environmental factors affecting estimation accuracy. A total of 265 Sentinel-1 SAR images acquired during 2015–2026 covering the USGS Thebes gauging station along the Mississippi River were analyzed using six VV- and VH-based backscatter metrics, yielding 1590 WSE estimates. Comparison with a conventional 1-m digital elevation model (DEM) revealed that its representation of river water-surface elevations at the time of the elevation survey, rather than submerged channel-bed elevations, limits its applicability for estimating WSE at low river stages. Among the six metrics, $\log_{10}$(VV) produced the best overall performance, with an RMSE of 1.61 m, mean error of −0.96 m, R^2 of 0.81, and percentage of lowest absolute error (PLE) of 44.5%. A sensitivity analysis using SAR image grid spacings of 10, 5, 2, and 1 m showed that $\log_{10}$(VV) maintained relatively stable estimation accuracy, whereas finer resampling did not consistently improve WSE estimates. Errors were smallest under low-flow conditions (WSE < 97.0 m), largest under medium- to high-flow

Academic Editors: Magaly Koch, Silvia Scifoni, Maria Marsella and Francesca Giannone

Received: 14 June 2026
Revised: 19 October 2026
Accepted: 30 October 2026
Published: 2 November 2026

Copyright: © 2026 by the author. Licensee MDPI, Basel, Switzerland. This article is an open access article distributed under the terms and conditions of the Creative Commons Attribution (CC BY) license.

conditions (97.0–102.5 m) and decreased again during flooding (WSE > 102.5 m). Analysis of 10 National Agricultural Imagery Program (NAIP) images revealed increasing vegetation along the inundation boundary above approximately 100 m WSE. Under medium- to high-flow conditions, calm conditions generally produced smaller errors than non-calm conditions, although errors did not increase monotonically with wind speed. E–W and SE–NW wind orientations generally produced larger errors than N–S and NE–SW orientations. These results indicate that WSE estimation accuracy reflects combined effects of vegetation, wind-generated water surface roughness, wind orientation, effective fetch, water depth, and river morphology. Although $\log_{10}$(VV) performed best overall, it provided the lowest absolute error for only 44.5% of acquisitions, highlighting the potential for condition-dependent backscatter metric selection to improve SAR-based river WSE retrieval.

Keywords: Sentinel-1 SAR; water surface elevation; river monitoring; synthetic aperture radar; inundation mapping; river inundation area; channel morphology; riparian vegetation; wind-induced waves; hydrological remote sensing

1. Introduction

River water surface elevation (WSE) relative to the mean sea level is an important hydrological variable indicating flow conditions in a river, e.g., low, medium, high, bankfull, and flooding. At a stream gauging station, the water surface height above the gage datum is called the river stage and monitored continuously. Adding the gage datum to the measured river stage yields the river WSE. Both river stage and river WSE can be used for estimating river discharge at gauging stations based on the stations' river stage or WSE versus discharge rating curves [1,2]. It is well established that river WSE (or stage) and discharge are essential hydrological variables for flood frequency analysis [3–5], flood prediction and prevention [6,7], water resources management [8,9], water cycle research [10,11], reservoir management [12], river navigation [13], riverine recreation [14], ecosystem services [15], and many other applications.

Although automatically measuring river stages or WSEs at gauging stations is effective and efficient, some operational costs (e.g., repairing and maintaining equipment, collecting and transferring data) are still necessary [16]. Insufficient funding has led to a decline in the number of gauging stations in the United States since the late 1990s [17–20]. Many major flood events globally were inadequately measured [21] as stream-gauging networks on large rivers have declined and there is an even more pronounced trend for medium and small rivers [20]. Missing data at gauging stations due to equipment failure, as well as the lack of river stage or WSE measurements at ungauged river cross-sections remain two major challenges faced by the hydrology and water resources community. To fill data gaps at gauging stations or to monitor WSEs at ungauged river cross-sections, remote sensing offers an economical, effective, and efficient approach that can play a significant role in addressing these challenges. Significant progress has been made in remote sensing of river stage since the 1990s [22–26].

As reported in the literature [27–32], there are two types of remote sensing approaches for monitoring river stage or WSE, i.e., directly measuring river WSEs using spaceborne or airborne LiDAR or radar altimetry [33–48], and indirectly estimating river WSEs from satellite imagery or aerial photos based on relationships between river width or inundation area versus river WSE, which are commonly established using topographic information [28–32,48–55]. Both methods have their own advantages and limitations. Although the direct method provides a straightforward way to measure river WSEs

without requiring additional remotely sensed or digital elevation model (DEM) data, conventional satellite radar altimetry is limited by sparse ground-track sampling and has generally been more applicable to relatively large rivers [56]. Even when satellites are overhead, if the radar or laser scanning points do not strike water surface at the river cross-sections of interest, no river WSE measurements can be obtained for those locations. One significant advantage of the direct method is its ability to measure WSE without requiring a DEM-derived inundation area–WSE relationship, although measurement accuracy varies with sensor characteristics, river width, and environmental conditions. Although the indirect method generally yields lower accuracy than the direct method, it offers the advantage of estimating river stage or WSE at locations where suitable remotely sensed imagery and sufficiently accurate, high-resolution topographic or topobathymetric elevation data are available. However, the applicability of this approach can be limited by the availability and quality of elevation data, particularly because accurate representation of riverbanks and floodplain topography is required to establish reliable relationships between inundation extent and WSE.

Both passive and active remote sensing techniques have been widely used to identify water bodies and to map river inundation, lakes, and wetlands. Each approach offers distinct advantages and limitations. Active microwave remote sensing is not constrained by cloud cover, weather conditions, or solar illumination. Because many flood events occur during or immediately after storm events under cloudy conditions—and because near-real-time river WSE information is critical for forecasting flood and issuing timely warnings to potentially affected communities—active microwave remote sensing is particularly valuable for flood mapping. Among active microwave remote sensing technologies, Synthetic Aperture Radar (SAR) is particularly effective for mapping the Earth's surface under all-weather, day-and-night conditions.

A recent major development in satellite-based water-surface monitoring is the Surface Water and Ocean Topography (SWOT) mission, which provides spatially extensive observations of WSE and other surface-water characteristics for rivers, lakes, and reservoirs. SWOT provides an important new capability for monitoring river WSE at large spatial scales and complements conventional gauging networks and other satellite-based approaches [57]. In comparison, SAR imagery provides relatively fine spatial detail for delineating water–land boundaries, which can be useful for indirectly estimating WSE from river inundation area–WSE relationships. Thus, SWOT and SAR-based approaches can be considered complementary, with their relative advantages depending on river width, channel morphology, spatial scale, and the specific objectives of WSE monitoring.

Indeed, numerous research efforts have focused on the application of SAR for mapping water bodies. A recent review by Guo et al. [58] analyzed approximately 136 studies published over the past thirty years and highlighted the methodological evolution from traditional machine learning to deep learning approaches. Many of these studies employed supervised image classification methods, which require training samples for both water and non-water classes. However, obtaining satisfactory results with supervised methods can be time-consuming. In contrast, unsupervised image classification methods could provide more rapid results, which is crucial for timely mapping of river inundation during flood events to save lives and minimize property damage. Therefore, further research on unsupervised SAR image classification for distinguishing water and non-water areas is warranted to advance the technique and improve the accuracy of river inundation estimates derived from SAR imagery.

Regarding the application of SAR imagery for estimating river WSEs using the indirect method, previous studies have demonstrated the potential of combining SAR-derived inundation boundaries with topographic elevation data to estimate floodwater levels and support hydraulic modeling [52–54,59]. However, WSE estimation accuracy

depends on both the delineation of river inundation areas and the reliability of the river inundation area–WSE (RIA–WSE) relationship derived from elevation data. For instance, even a small error in the SAR-estimated inundation area may produce a substantial WSE error along steep riverbanks, where small changes in inundation extent correspond to large elevation differences. In addition, SAR image grid spacing and threshold selection for unsupervised SAR image classification may influence inundation-area delineation and subsequent WSE estimation. Although previous studies have investigated uncertainties in SAR-derived floodwater levels, the effects of vegetation, wind-generated water surface roughness, and river morphology on WSE estimation accuracy under different flow conditions remain insufficiently understood. Therefore, this study evaluates the effects of DEM characteristics, SAR image grid spacing, and threshold selection on WSE estimation accuracy and addresses the following research questions: (1) How does riparian vegetation affect Sentinel-1 SAR backscattering and introduce bias in WSE estimation? (2) How do wind speed, wind orientation relative to the river channel, and effective fetch affect Sentinel-1 SAR backscattering and associated WSE estimation errors through wind-generated water surface roughness? (3) What roles do channel cross-sectional geometry and riverbank slope play in controlling WSE retrieval accuracy? By addressing these questions, this study investigates the methodological, environmental, and geomorphic factors influencing SAR-derived WSE errors and provides practical guidance for improving SAR-based river WSE estimation.

The accuracy of SAR imagery-based river WSE retrieval is evaluated in this study by comparing SAR-estimated WSEs with measured WSEs at a stream gauging station. Unlike multispectral satellite imagery, such as Landsat 8/9 Operational Land Imager (OLI) and Sentinel-2 Multispectral Instrument (MSI), or aerial photographs that record surface reflectance in the visible and near-infrared wavelengths and can be used to calculate various water indices [60], e.g., NDWI [61], MNDWI [62], and AWEI [63], spaceborne or airborne SAR systems emit microwave pulses toward the Earth's surface and measure the returned signals, referred to as backscatter, to produce SAR imagery. Because no single SAR-based water index has been widely established for distinguishing water from non-water pixels, this study evaluates multiple SAR backscatter metrics derived from co-polarized (VV) and cross-polarized (VH) backscatter for water classification. The Otsu algorithm [32,64–67] is used to determine an optimal threshold for separating water and non-water pixels for each backscatter metric. The six backscatter metrics and their application to RIA and WSE estimation are described in Section 3.

The arrangement of this paper is as follows. Section 2 describes the study area and data. Section 3 introduces methods for preprocessing SAR imagery, constructing RIA-WSE rating relationships, deriving optimal SAR backscatter thresholds, and estimating RIAs and WSEs. Results, discussion, and conclusions are presented in Sections 4, 5, and 6, respectively.

2. Materials

The streamflow gauging station on the upper Mississippi river at Thebes, Illinois (USGS station 07022000; 37.22025°N, 89.46317°W, gage datum = 91.35 m above NAVD88), managed by the U.S. Geological Survey (USGS), was selected for this study (Figure 1). A 2-m-resolution topobathymetric elevation model (TEM) data was obtained from the Upper Mississippi River System (UMRS) Topobathy dataset developed by the USGS in cooperation with the U.S. Army Corps of Engineers (USACE) [68,69]. The dataset provides a seamless representation of floodplain and riverbed elevations by merging terrestrial lidar data with river bathymetry. The original lidar and bathymetric data were collected at 1-m and 5-m resolutions, respectively, and the bathymetric mapping methodology is described in [70]. A single numerical vertical accuracy is not reported for the merged

Topobathy product; according to the dataset metadata, no adjustments were made to alter the original vertical accuracies of the lidar and bathymetric data. In areas where bathymetric observations were unavailable, interpolation was used, and portions of the main channel without bathymetric data were represented by water-surface elevations from hydroflattened DEMs, which may introduce additional uncertainty in the resulting elevation surface.

For comparison, a conventional 1-m-resolution DEM data was obtained from the USGS 3D Elevation Program (3DEP) through The National Map Downloader. Unlike the 2-m TEM, the conventional DEM does not incorporate submerged channel bathymetry. The 1-m DEM data was used only to construct an alternative RIA–WSE relationship and evaluate the influence of DEM selection on WSE estimates derived from NAIP imagery.

The Mississippi River at Thebes drains a large upstream area of approximately 1.85×10^6 km^2 and experiences substantial variations in river discharge and stage, providing a wide range of hydrologic conditions for evaluating SAR-based WSE estimation. The study reach includes a well-defined river channel and adjacent floodplain with substantial topographic variation (Figure 1), making it suitable for examining how river morphology and changing inundation extent affect SAR-derived WSE accuracy.

This study first validated the accuracy of the constructed RIA-WSE relationship through comparing measured WSEs with estimated WSEs based on estimated RIAs using 15 high spatial resolution aerial images acquired by National Agricultural Imagery Program (NAIP) between 2009 and 2024. The spatial resolution of the NAIP imagery was 1 m prior to 2018, 0.6 m during 2018–2022, and 0.3 m after 2022. Gage height at the Thebes station was recorded at 1-h intervals before 6 June 2011, and at 30-min intervals thereafter. The USGS accuracy standard for stage measurements is ±0.003 m or 0.2% of the effective stage, whichever is larger [71].

The SAR instruments aboard the European Space Agency's Sentinel-1A/B satellites provide all-weather, day-and-night observations at a frequency of 5.405 GHz (C-band), with dual-polarization modes (VV/VH). In this study, 265 Sentinel-1 Level-1 Ground Range Detected (GRD) products covering the Thebes gauging station from 27 May 2015, to 28 August 2026, were downloaded from the Alaska Satellite Facility (ASF). All images used in this study were acquired in VV/VH dual-polarization mode and processed at a 10-m pixel spacing. For validation, the WSE derived from the gage-height measurement closest in time to each Sentinel-1 acquisition was compared with the corresponding SAR-estimated WSE.

To assess impacts of wind speed and direction on the accuracy of the SAR estimated WSEs, five-minute Automated Surface Observing System (ASOS) observations from the Cape Girardeau FAA Airport (KCGI; 37.22532°N, 89.57076°W; elevation 104 m) were used to obtain wind speed and direction. This weather station is the nearest weather station to the study area, located approximately 10 km west of the Thebes gauging station in a straight-line distance (Figure 1).

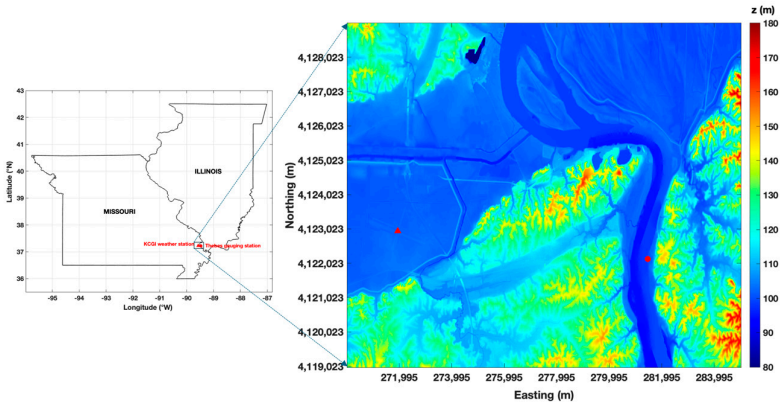


Figure 1. Elevation of the study area and surrounding area, showing the locations of the Thebes gauging station (red dot) and the KCGI weather station (red triangle).

3. Methods

3.1. Preprocess Sentinel-1 SAR Images

Sentinel-1 GRD SAR data were preprocessed using the Sentinel Application Platform (SNAP) developed by European Space Agency [72]. The preprocessing workflow generally followed the Sentinel-1 GRD preprocessing procedure described in [73] and consisted of seven steps: (1) Applying orbit file to improve the geolocation accuracy of the SAR imagery; (2) Spatially subsetting each SAR scene around the Thebes gauging station, using the geographic coordinates (see Section 2) of the gauging station as the center of the subset. The spatial extent was defined as ±0.05° in both latitude and longitude from the station, resulting in a 0.10° × 0.10° area; (3) Removing thermal noise in the SAR observations; (4) Performing radiometric calibration on the SAR measurements with Beta Nought (β^0) selected as the calibrated backscatter output; (5) Radiometric terrain flattening was then applied to adjust the terrain-induced variations in radar illumination and to produce Gamma Nought (γ^0) backscatter; (6) The γ^0 backscatter data were subsequently filtered using the Refined Lee Speckle filter to reduce speckle noise while preserving important spatial features and backscatter variations; (7) Geometric terrain correction was performed using the SRTM 1-s HGT (Auto Download) DEM dataset to compensate for terrain-induced geometric distortions. The terrain-corrected γ^0 data were projected to the WGS84/UTM Zone 16N coordinate reference system with a 10-m pixel spacing and subsequently used to delineate river inundation areas.

Following SNAP preprocessing, the terrain-corrected γ^0 SAR images were further processed in ArcGIS Pro (version 3.2.0). Each image was clipped to a 2 km × 2 km area centered on the Thebes gauging station, extending 1000 m in each direction from the station in the UTM coordinate system. The clipped SAR images, originally having a 10-m pixel spacing, were subsequently resampled to a 1-m grid using bilinear interpolation. For the grid-spacing sensitivity analysis, the original 10-m images and images resampled to 5-, 2-, and 1-m grids were evaluated to assess the effects of grid spacing and threshold selection on WSE estimation accuracy.

3.2. Construct River Inundation Area—Water Surface Elevation Rating Curve

The TEM data were used to construct the RIA–WSE rating curve within the predefined polygon. Starting from the minimum TEM elevation within the polygon, the WSE was progressively increased at an increment of 0.01 m over a 40-m elevation range. At each elevation level, the corresponding RIA was calculated from the TEM data, producing a series of RIA–WSE data pairs. These data pairs were used to construct the

RIA–WSE rating curve, which shows how RIA changes with WSE and reveals variations in the slope of the relationship associated with channel and floodplain geometry. No mathematical function was fitted to the RIA–WSE data pairs. For WSE retrieval, the original RIA–WSE data pairs were retained, and linear interpolation (Equation (1)) was used to estimate WSE from the RIA determined from each SAR image.

$$WSE = WSE_i + \frac{(WSE_{i+1} - WSE_i)}{(RIA_{i+1} - RIA_i)}(RIA - RIA_i), if\ RIA_i \le RIA < RIA_{i+1} \quad (1)$$

Because the RIA–WSE relationship was derived from raster elevation data, multiple consecutive WSE levels could correspond to the same RIA. Linear interpolation was performed only over intervals with increasing RIA values, as specified in Equation (1), thereby avoiding division by zero.

3.3. Estimate River Inundation Area Using the NAIP Aerial Imagery

A supervised image classification method, the modified K-Nearest Neighbor (KNN) method [32,60,74], was applied to the near-infrared (NIR) band of the 15 NAIP aerial images to classify water and non-water pixels. For each NAIP aerial image, two training sample sets representing water and non-water classes were selected by visual inspection with high confidence. Each training set covered a 40 × 40-pixel rectangular area. To determine whether an unknown pixel x belonged to water or non-water class, the absolute NIR reflectance differences between pixel x and each of the water and non-water training pixels were calculated as follows:

$$SD_{wi} = |NIR_x - NIR_{wi}|,\ SD_{nwi} = |NIR_x - NIR_{nwi}| \quad (2)$$

where SD_{wi} and SD_{nwi} are the absolute NIR reflectance differences between pixel x and water training pixel i and non-water training pixel i, respectively; and NIR_x, NIR_{wi}, and NIR_{nwi} are NIR reflectance values of pixel x, water training pixel i, and non-water training pixel i (i = 1, .., 1600), respectively. The sums of the inverse absolute NIR reflectance differences between pixel x and all water training pixels (ISD_w) and all non-water training pixels (ISD_{nw}) were then computed as follows:

$$ISD_w = \sum_{i=1}^{i=1600}\left(\frac{1}{SD_{wi}}\right),\ ISD_{nw} = \sum_{i=1}^{i=1600}\left(\frac{1}{SD_{nwi}}\right) \quad (3)$$

To avoid division by zero when computing ISD_w and ISD_{nw}, the minimum non-zero absolute NIR reflectance difference (SD_{min}) among all differences between pixel x and all the training pixels was first determined. When an absolute NIR reflectance difference was zero, its inverse was assigned a value of $2/SD_{min}$. If $ISD_w > ISD_{nw}$, pixel x was classified as water, otherwise, it was classified as non-water. The inundation area within the predefined polygon was then calculated by multiplying the number of pixels classified as water by the area of a single NAIP aerial image pixel.

3.4. Estimate River Inundation Area in SAR Imagery Using the Otsu Method

Six SAR backscatter metrics were evaluated in this study: $\log_{10}(VH)$, $\log_{10}(VV)$, $\log_{10}[(VH + VV)/2]$, $\log_{10}[(VH \times VV)^{0.5}]$, $\log_{10}[(VH^2 + VV^2)^{0.5}]$, and $\log_{10}[2/(1/VH + 1/VV)]$. For each Sentinel-1 SAR image, the Otsu method was applied independently to each of the six backscatter metrics to determine the optimal threshold for separating water and non-water pixels.

The Otsu method [64] was first proposed in 1979 to determine an optimal threshold for separating image pixels into two classes, i.e., objects and background, in a gray-level image through maximizing inter-class variance. In this study, the two image classes are water and non-water, and the optimal threshold for separating them was obtained through achieving the maximum value of an objective function *f* defined as follows:

$$f = P_w P_{nw} (\mu_w - \mu_{nw})^2 \quad (4)$$

where P_w and P_{nw} are probabilities of water and non-water pixels, respectively, and μ_w and μ_{nw} are mean backscatter values of classified water and non-water pixels, respectively. Since the magnitude of $\log_{10}$(VH) is in the range of (−5, −1), while $\log_{10}$(VV) is in the range of (−4, 0), the optimal backscatter value was determined through iterating the backscatter threshold between −5 and 0 with an interval of 0.01 to achieve the maximum value of the objective function as shown in Equation (4). All terms on the right-hand side of Equation (4) were calculated as follows:

$$P_w = \frac{n_w}{n},\ P_{nw} = \frac{n_{nw}}{n}, \mu_w = \frac{\sum_{i=1}^{i=n_w} \sigma_i}{n_w},\ \mu_{nw} = \frac{\sum_{i=1}^{i=n_{nw}} \sigma_i}{n_{nw}} \quad (5)$$

where σ_i is the backscatter of pixel i, n, n_w and n_{nw} are the number of total pixels, number of pixels with a backscatter value less than σ_o, number of pixels with a backscatter value greater than or equal to σ_o inside the predefined polygon, respectively, and σ_o is the optimal backscatter threshold.

3.5. Evaluate Accuracy of the Estimated River Water Surface Elevations

The accuracy of the estimated WSEs is evaluated based on three errors, i.e., mean error (ME), mean absolute error (MAE), and root mean square error (RMSE), and the coefficient of determination (R^2), as given as follows:

$$\boldsymbol{ME} = \frac{\sum_{i=1}^{n}(\boldsymbol{WSE_i'} - \boldsymbol{WSE_i^*})}{\boldsymbol{n}}, \boldsymbol{MAE} = \frac{\sum_{i=1}^{n}|\boldsymbol{WSE_i'} - \boldsymbol{WSE_i^*}|}{\boldsymbol{n}}, \boldsymbol{RMSE} = \sqrt[2]{\frac{\sum_{i=1}^{n}(\boldsymbol{WSE_i'} - \boldsymbol{WSE_i^*})^2}{\boldsymbol{n}}}$$

$$\boldsymbol{R^2} = \frac{\{\sum_{i=1}^{n}[(\boldsymbol{WSE_i'} - \overline{\boldsymbol{WSE'}})(\boldsymbol{WSE_i^*} - \overline{\boldsymbol{WSE^*}})]\}^2}{\sum_{i=1}^{n}[(\boldsymbol{WSE_i'} - \overline{\boldsymbol{WSE'}})^2]\sum_{i=1}^{n}[(\boldsymbol{WSE_i^*} - \overline{\boldsymbol{WSE^*}})^2]} \quad (6)$$

where $\boldsymbol{WSE_i'}$ and $\boldsymbol{WSE_i^*}$ are estimated and measured WSE, respectively, i = 1, .., n, n is number of measurements, $\overline{\boldsymbol{WSE'}}$ and $\overline{\boldsymbol{WSE^*}}$ are mean estimated and measured WSE, respectively.

4. Results

4.1. The Constructed RIA-WSE Rating Curve and Its Accuracy

The clipped TEM data surrounding the Thebes gauging station, extending ±1000 m in both easting and northing directions from the station, are shown in Figure 2a. The predefined polygon (white outline), encompassing the gauging station and portions of the river channel and adjacent floodplain, and the gauging station location (red dot) are also shown in Figure 2a. The polygon extends approximately 110 m parallel to the riverbanks and 554 m perpendicular to the riverbanks, corresponding to 55 × 277 grid cells at the 2-m horizontal resolution of the TEM.

Using the method described in Section 3.2, the RIA–WSE rating curve was constructed from the 2-m TEM data within the predefined polygon (Figure 2b). For comparison, an additional RIA–WSE relationship was constructed using the conventional 1-m DEM data within the same polygon. The two relationships exhibit close agreement at higher water levels but differ substantially below approximately 97.3 m. In particular, the 1-m DEM-derived relationship exhibits a horizontal segment at approximately 95.72 m because the conventional DEM represents the river surface at approximately the water level during the elevation survey rather than the submerged channel-bed elevations, limiting its ability to resolve WSE variations at low river stages.

Both the TEM- and DEM-derived RIA–WSE relationships exhibit a pronounced change in slope near a WSE of approximately 102.5–103.0 m (Figure 2b), close to the estimated bankfull elevation of 102.5 m. Below this elevation, inundation is largely

confined to the river channel, where relatively steep banks limit the lateral expansion of the inundated area. As WSE approaches and exceeds the bankfull elevation, inundation may extend into adjacent lower-gradient areas, causing RIA to increase more rapidly with increasing WSE. This transition in the rate of inundation-area expansion produces the pronounced knee in the rating curve.

To assess the accuracy of the constructed RIA–WSE relationships, 15 NAIP aerial images covering the study area were downloaded from USGS EarthExplorer. River inundation areas were extracted from these images using the modified KNN classification method described in Section 3.3, and the resulting RIAs were converted to WSE using the relationships derived from the 2-m TEM and conventional 1-m DEM. Because the exact acquisition times of the NAIP images were unavailable, USGS WSE measurements recorded at approximately 12:00 local time on the corresponding acquisition dates were used for comparison. Table 1 presents the NAIP image acquisition dates, WSEs measured at the Thebes gauging station at approximately 12:00 local time on those dates, estimated WSEs using the two relationships, and the differences between estimated and measured WSEs.

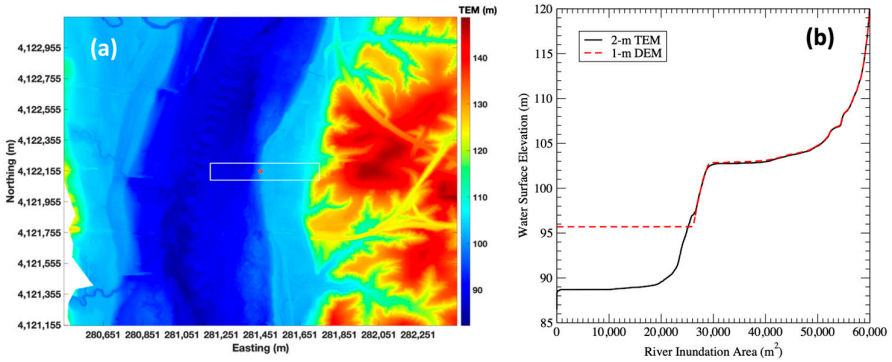


Figure 2. (**a**) Topobathymetric elevation model (TEM) surrounding the Thebes gauging station, showing the predefined polygon (white outline) and gauging station location (red dot). (**b**) River inundation area–water surface elevation (RIA–WSE) relationships derived from the 2-m TEM (black solid line) and conventional 1-m DEM (red dashed line).

Table 1. Acquisition dates of 15 NAIP images, WSEs measured at the Thebes gauging station, WSEs estimated using RIA–WSE relationships derived from the 2-m TEM and conventional 1-m DEM, and corresponding estimation errors.

AD	WSE* (m)	WSE′ (m)	WSE′ – WSE* (m)	WSE# (m)	WSE# – WSE* (m)	AD	WSE* (m)	WSE′ (m)	WSE′ – WSE* (m)	WSE# (m)	WSE# – WSE* (m)
19 Jun 2009	101.14	101.55	0.41	101.61	0.47	19 Jun 2017	98.90	98.47	−0.43	98.33	−0.57
18 Jun 2010	101.51	101.64	0.13	101.66	0.15	20 Sep 2018	100.22	100.24	0.02	100.31	0.09
1 Jul 2010	102.88	102.82	0.06	102.98	0.10	16 Sep 2019	98.75	98.43	−0.32	98.25	−0.50
12 Aug 2011	99.59	99.73	0.14	99.69	0.10	22 Jun 2021	96.18	96.88	0.70	95.72+	−0.46
13 Jun 2012	96.40	97.31	0.91	96.68	0.28	15 Jun 2022	99.21	99.98	0.77	100.07	0.86
5 Jul 2014	100.52	100.80	0.28	100.90	0.38	17 Aug 2023	95.27	96.19	0.92	95.72 +	0.45
22 Jul 2014	99.97	100.43	0.46	100.59	0.62	22 Aug 2024	96.80	97.24	0.44	96.42	−0.38
18 Jun 2016	98.48	98.55	0.07	98.41	−0.07						

Note: AD denotes acquisition date; WSE* denotes the measured water surface elevation at the Thebes gauging station; WSE′ and WSE# denote WSE estimated using the RIA–WSE relationships derived from the 2-m topobathymetric elevation model (TEM) and conventional 1-m digital elevation model (DEM), respectively. + indicates that the estimated WSE reached the lower bound

of 95.72 m imposed by the 1-m DEM-derived RIA–WSE relationship, which cannot resolve lower water levels because submerged channel bathymetry is not represented.

The TEM-derived relationship yielded a mean error (ME) of 0.30 m, a root mean square error (RMSE) of 0.50 m, and an R^2 of 0.98. The conventional DEM-derived relationship produced slightly smaller overall errors, with an ME of 0.10 m and an RMSE of 0.43 m. However, two DEM-derived WSE estimates, corresponding to 22 June 2021, and 17 August 2023, reached the lower estimation limit of 95.72 m despite different measured WSEs of 96.18 and 95.27 m, respectively (Table 1). This limitation reflects the absence of submerged channel bathymetry in the conventional DEM and its inability to resolve WSE variations at sufficiently low river stages. Therefore, although the 1-m DEM-derived relationship yielded a slightly lower overall RMSE for the 15 NAIP images, the 2-m TEM-derived relationship was retained for all Sentinel-1 SAR-based WSE estimates because it incorporates submerged channel bathymetry and can represent a broader range of river stages, including lower stages that cannot be resolved using the conventional DEM.

To further examine the characteristics of the TEM-based WSE estimation errors, Figure 3a compares the estimated and measured WSEs, while Figure 3b presents the NAIP-derived RIAs against measured WSEs together with the TEM-derived RIA–WSE rating curve. Table 1 and Figure 3a,b indicate that the estimated WSEs generally agree well with gauge measurements at higher river stages, particularly above 98.0 m. However, positive estimation errors occurred for all four NAIP observations with measured WSE ≤ 97.3 m. To investigate these discrepancies, three NAIP images associated with relatively large WSE overestimations, acquired on 13 June 2012 (measured WSE = 96.40 m; estimated WSE = 97.31 m), 22 June 2021 (measured WSE = 96.18 m; estimated WSE = 96.88 m), and 17 August 2023 (measured WSE = 95.27 m; estimated WSE = 96.19 m), are shown in Figure 4. The predefined polygon and the water–land boundaries delineated using the modified KNN classification of the NAIP NIR images are also shown in Figure 4.

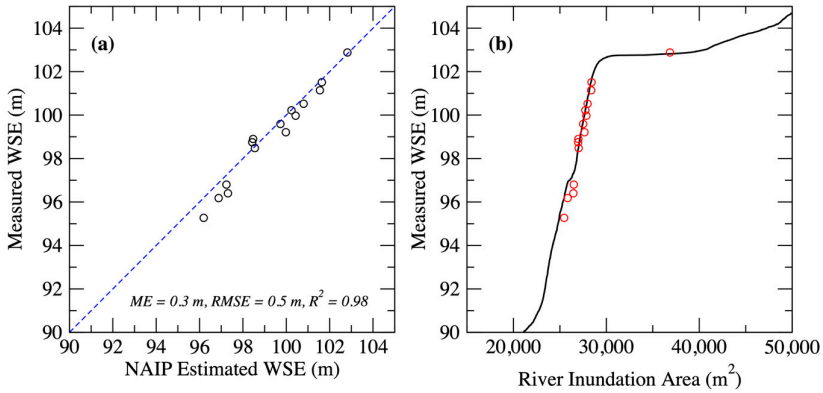


Figure 3. (**a**) Comparison between NAIP-estimated and USGS gauge-measured WSEs. The dashed line represents the 1:1 relationship. (**b**) RIA–WSE rating curve calculated directly from the TEM (black curve) and independent observations of NAIP-derived RIAs and corresponding USGS gauge-measured WSEs (red circles). The NAIP observations are used to evaluate the TEM-derived relationship and are not used to construct or fit the rating curve.

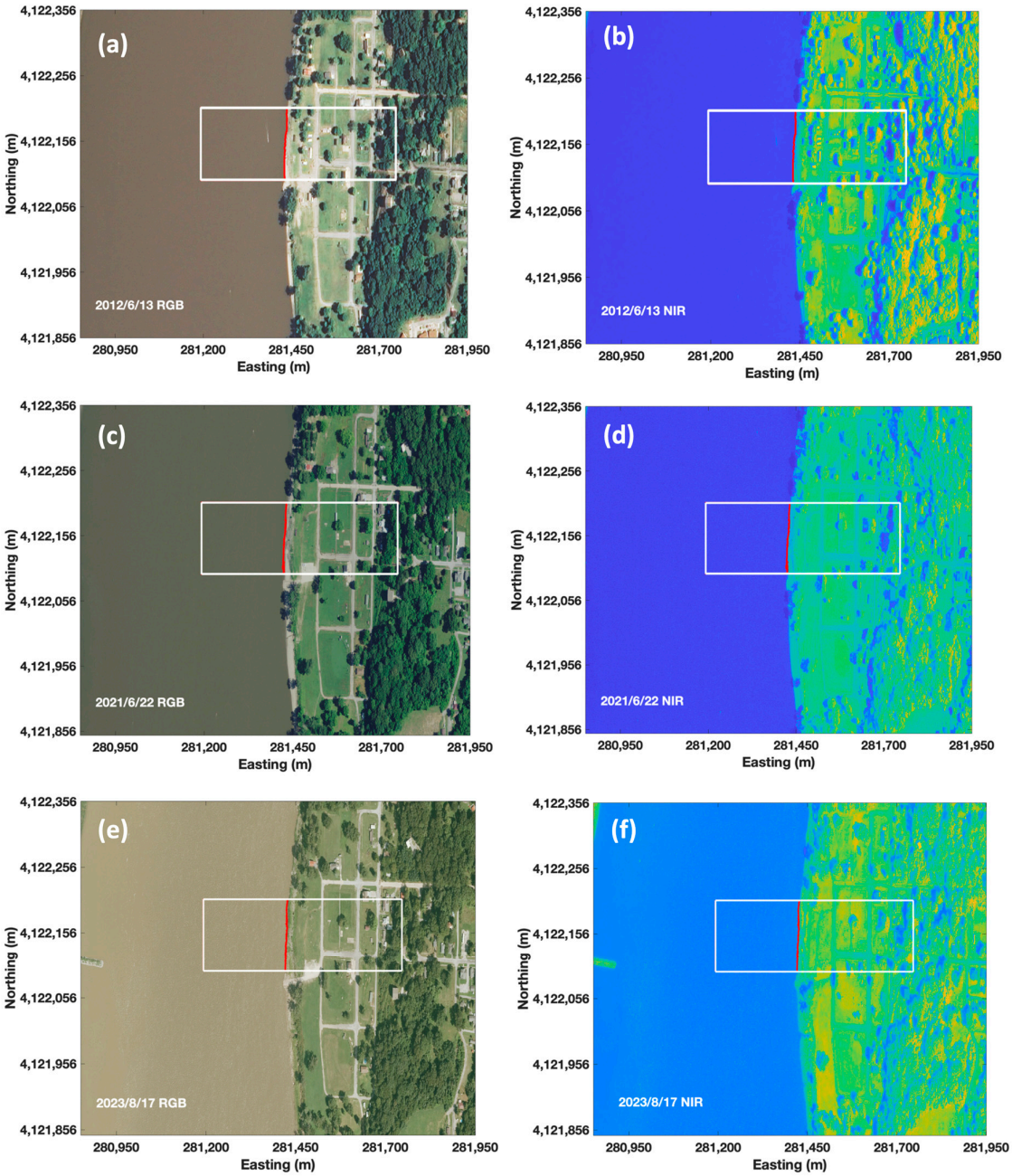


Figure 4. National Agriculture Imagery Program (NAIP) RGB and near-infrared (NIR) images acquired on (**a**,**b**) 13 June 2012, (**c**,**d**) 22 June 2021, and (**e**,**f**) 17 August 2023. The white rectangles indicate the predefined RIA analysis polygon (110 m × 554 m), and the red lines represent the water–land boundaries delineated from the NAIP imagery.

Sun glint is evident on the river water surface in the RGB and NIR images acquired on 17 August 2023 (Figure 4e,f). Sun glint can increase the spectral reflectance of some water training samples, thereby reducing the spectral contrast between water and non-water samples and causing the KNN classifier to misclassify some land pixels adjacent to the water–land boundary as water. The resulting overestimation of RIA can consequently lead to an overestimation of WSE. In contrast, the water surfaces on 13 June 2012 (Figure 4a,b) and 22 June 2021 (Figure 4c,d) appeared calm, with no noticeable sun glint or waves. Visual inspection indicates that water and non-water pixels were generally classified

accurately on 13 June 2012, whereas the extracted water–land boundary on 22 June 2021, was slightly shifted toward the river side relative to the visually identified boundary, indicating a slight underestimation of RIA. Because RIA increases monotonically with WSE, an underestimated RIA would be expected to produce an underestimated rather than overestimated WSE. Thus, KNN-derived RIA errors alone cannot fully explain the WSE overestimation observed on these two dates.

The comparison between the 2-m TEM-derived and conventional 1-m DEM-derived RIA–WSE relationships provides additional evidence of sensitivity to DEM selection at low river stages. For the four NAIP images with measured WSE ≤ 97.3 m, the TEM-derived estimates consistently exceeded the gauge measurements, with an ME of 0.74 m and an RMSE of 0.77 m, whereas the conventional DEM-derived estimates yielded an ME of −0.03 m and an RMSE of 0.40 m. These differences suggest that uncertainty in the low-stage portion of the TEM-derived RIA–WSE relationship may contribute to the observed WSE overestimation. However, the conventional DEM does not adequately represent submerged channel bathymetry, and two of its WSE estimates were constrained to the lower limit of 95.72 m. Therefore, its smaller estimation errors do not necessarily indicate a more accurate representation of low-stage inundation conditions. Furthermore, the exact acquisition times of the NAIP images were unavailable, and the USGS WSE measurements at approximately 12:00 local time may not correspond exactly to river stages at the time of NAIP acquisition. Short-term stage changes associated with this temporal mismatch may also contribute to the observed discrepancies. Overall, the positive WSE errors at low stages may reflect a combination of uncertainty in NAIP-derived RIAs, sensitivity to the TEM-derived RIA–WSE relationship, and temporal differences between image acquisition and gauge observations.

4.2. Assessment of the Accuracy of SAR-Estimated WSEs

Applying the SAR preprocessing procedures to each image produced two clipped, radiometrically and geometrically corrected, and resampled backscatter images corresponding to the VH and VV polarizations. The Otsu method was then applied to determine the optimal threshold for each of six backscatter metrics: $\log_{10}(VH)$, $\log_{10}(VV)$, $\log_{10}[(VH + VV)/2]$, $\log_{10}[(VH * VV)^{0.5}]$, $\log_{10}[(VH^2 + VV^2)^{0.5}]$, and $\log_{10}[2/(1/VH + 1/VV)]$. These thresholds were used to separate water and non-water pixels. For each SAR image, the six backscatter metrics produced six corresponding RIA estimates within the predefined polygon, which were subsequently converted to six WSE estimates using the constructed RIA–WSE rating curve. To illustrate the water–land boundary delineation using the six backscatter metrics, Figure 5 shows the results within the predefined polygon for the Sentinel-1 SAR image acquired on 27 September 2019.

By substituting the 1590 estimated RIAs derived from 265 SAR images using the six backscatter metrics into the established RIA-WSE relationship, a total of 1590 WSE estimates were obtained. The accuracy of these estimates was evaluated using the mean error (ME), root mean square error (RMSE), coefficient of determination (R^2), and percentage of lowest absolute error (PLE). PLE represents the percentage of the 265 SAR images for which a given backscatter metric achieved the lowest absolute WSE estimation error among the six metrics. When two or more metrics yielded the same lowest absolute error for an individual SAR image, each was counted toward its respective PLE. Therefore, the sum of the PLE values can exceed 100%. The resulting accuracy statistics are summarized in Table 2. To further compare the performance of the six backscatter metrics, Figure 6 presents box plots of their accuracy rankings (with 1 indicating the highest accuracy and 6 the lowest) and WSE estimation errors (WSE′ − WSE*).

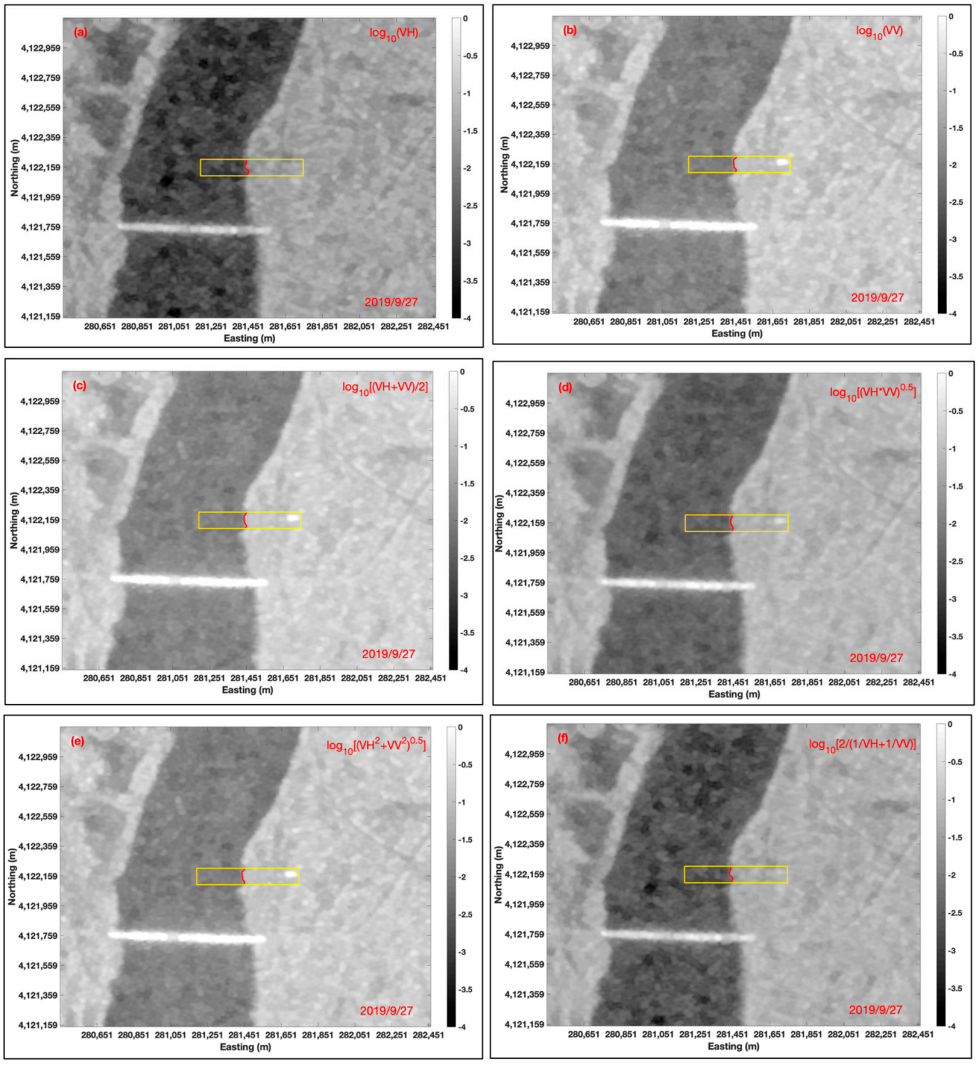


Figure 5. Sentinel-1 SAR backscatter images acquired on 27 September 2019, for the six backscatter metrics: (**a**) $\log_{10}(VH)$, (**b**) $\log_{10}(VV)$, (**c**) $\log_{10}[(VH + VV)/2]$, (**d**) $\log_{10}[(VH * VV)^{0.5}]$, (**e**) $\log_{10}[(VH^2 + VV^2)^{0.5}]$, and (**f**) $\log_{10}[2/(1/VH + 1/VV)]$. The predefined polygon is shown in yellow, and the extracted water–land boundaries are shown in red.

Table 2. Error statistics of the SAR-estimated water surface elevations (WSEs).

	$\log_{10}(VH)$	$\log_{10}(VV)$	$\log_{10}[(VH + VV)/2]$	$\log_{10}[(VH * VV)^{0.5}]$	$\log_{10}[(VH^2 + VV^2)^{0.5}]$	$\log_{10}[2/(1/VH + 1/VV)]$
ME (m)	−1.09	−0.96	−0.99	−1.05	−0.97	−1.06
RMSE (m)	1.89	1.61	1.65	1.72	1.63	1.82
R^2	0.73	0.81	0.81	0.80	0.81	0.76
PLE (%)	27.6	44.5	9.4	10.2	17.7	11.3

Note: Number of samples is 265; PLE indicates percentage of the lowest absolute error.

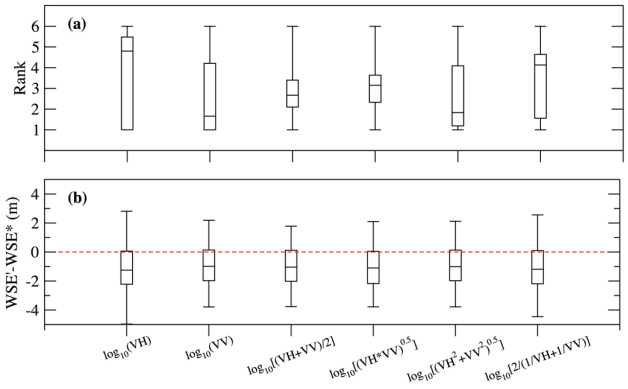


Figure 6. (**a**) Boxplot of the accuracy ranking of the SAR estimated WSEs, (**b**) boxplot of the error of the SAR-estimated WSEs. The red dashed line indicates WSE′ − WSE* = 0.

Both Table 2 and Figure 6 indicate that $\log_{10}$(VV) generally produced the most accurate WSE estimates among the six backscatter metrics. It yielded the lowest RMSE (1.61 m), the highest R^2 (0.81, tied with two combined metrics), and the highest PLE (44.5%). Thus, $\log_{10}$(VV) achieved the lowest absolute WSE estimation error for 44.5% of the 265 SAR images, indicating that it more frequently provided the most accurate WSE estimate than the other five backscatter metrics. VV polarization is particularly responsive to differences in surface roughness and dielectric properties between open water and surrounding land surfaces, which can facilitate delineation of the water–land boundary. The strong performance of VV polarization for water detection is also consistent with findings reported in previous studies [65–67].

Table 2 and Figure 6 further show that the performance of $\log_{10}[(VH^2 + VV^2)^{0.5}]$ was very similar to that of $\log_{10}$(VV), with an ME of −0.97 m, RMSE of 1.63 m, and R^2 of 0.81, compared with −0.96 m, 1.61 m, and 0.81, respectively, for $\log_{10}$(VV). However, its PLE was substantially lower (17.7%) than that of $\log_{10}$(VV) (44.5%). Because the magnitude of VV backscatter is typically much greater than that of VH, the VV component tends to dominate the combined term $(VH^2 + VV^2)^{0.5}$. Consequently, $\log_{10}[(VH^2 + VV^2)^{0.5}]$ behaves similarly to $\log_{10}$(VV), explaining their comparable overall WSE estimation error statistics despite the substantial difference in PLE.

Nevertheless, the PLE of 44.5% for $\log_{10}$(VV) indicates that VV did not provide the lowest absolute WSE error for every SAR acquisition. In comparison, $\log_{10}$(VH), despite its higher overall RMSE of 1.89 m, provided the lowest absolute WSE error for 27.6% of the acquisitions. The different responses of VV and VH to water-surface roughness and vegetation backscattering suggest that their relative performance may vary with flow regime, wind conditions, and vegetation along the water–land boundary. These complementary responses indicate the potential for a multi-polarization strategy that combines or conditionally selects VV and VH information rather than relying exclusively on a single polarization. However, a larger dataset would be needed to establish and validate reliable condition-specific selection criteria.

4.3. Sensitivity of SAR-Estimated WSEs to Image Grid Spacing and Threshold Selection

To assess the sensitivity of SAR-derived WSE estimates to image grid spacing and threshold selection, the original 10-m Sentinel-1 SAR images and images resampled to 5-, 2-, and 1-m grids using bilinear interpolation were analyzed for all 265 acquisitions. Two threshold-selection approaches were evaluated. In the first approach, thresholds were independently determined for each SAR image at each grid spacing using the Otsu method. In the second approach, thresholds determined from the corresponding 1-m

images were applied to the images at the coarser grid spacings. For both approaches, river inundation areas (RIAs) were delineated using the six backscatter metrics and converted to WSE using the same TEM-derived RIA–WSE rating curve. Figure 7 compares the resulting root mean square errors (RMSEs) across the four grid spacings.

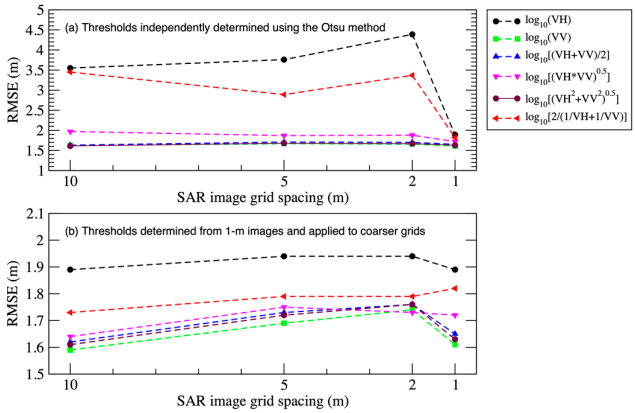


Figure 7. Sensitivity of Sentinel-1 SAR-derived WSE estimates to SAR image grid spacing and threshold selection for six backscatter metrics. (**a**) Thresholds independently determined for each image at each grid spacing using the Otsu method. (**b**) Thresholds determined from the corresponding 1-m images using the Otsu method and applied to the coarser grids. RMSEs were calculated by comparing SAR-derived WSE estimates with corresponding measurements at the Thebes gauging station.

When thresholds were independently determined at each grid spacing (Figure 7a), the RMSEs of $\log_{10}(VV)$, $\log_{10}[(VH + VV)/2]$, and $\log_{10}[(VH^2 + VV^2)^{0.5}]$ varied only slightly, ranging from 1.61 to 1.67 m, 1.63 to 1.71 m, and 1.61 to 1.68 m, respectively. In contrast, $\log_{10}(VH)$ exhibited substantially greater variations, with RMSEs of 3.55, 3.76, 4.39, and 1.89 m at grid spacings of 10, 5, 2, and 1 m, respectively. The harmonic-mean metric, $\log_{10}[2/(1/VH + 1/VV)]$, showed a similar pattern, with RMSEs of 3.45, 2.89, 3.37, and 1.82 m, respectively. These results indicate that the sensitivity of WSE estimation accuracy to image grid spacing differs considerably among the backscatter metrics.

When thresholds determined from the 1-m images were applied to the coarser grids (Figure 7b), the RMSE variations were substantially reduced for $\log_{10}(VH)$ and the harmonic-mean metric. For $\log_{10}(VH)$, RMSE ranged from 1.89 to 1.94 m across the four grid spacings, compared with 1.89~4.39 m when thresholds were independently determined. Similarly, the RMSE of the harmonic-mean metric ranged from 1.73 to 1.82 m, compared with 1.82~3.45 m under independent threshold selection. For $\log_{10}(VV)$, RMSE ranged from 1.59 to 1.74 m, indicating relatively small differences among grid spacings under both threshold-selection approaches. These results suggest that differences in threshold selection contributed substantially to the greater sensitivity of $\log_{10}(VH)$ and the harmonic-mean metric observed in Figure 7a.

Overall, the results indicate that the sensitivity of SAR-derived WSE estimates to image grid spacing depends on both the backscatter metric and the threshold-selection procedure. Although finer grid spacing did not consistently produce lower WSE estimation errors, $\log_{10}(VV)$ maintained relatively low and stable RMSEs across all four grid spacings under both threshold-selection approaches, further supporting its robustness for SAR-based WSE estimation. Resampling to finer grids allows water–land boundaries and inundation areas to be represented at smaller spatial increments but increases computational time and memory requirements without increasing the intrinsic spatial resolution of Sentinel-1 observations. Therefore, the selection of SAR image grid

spacing should balance the desired spatial discretization of inundation boundaries against computational efficiency, as finer resampling does not necessarily improve WSE estimation accuracy.

5. Discussion

5.1. Error Characteristics of SAR-Estimated WSEs

To further examine the error characteristics of the SAR-estimated WSEs, Figure 8 shows scatter plots of the SAR-estimated WSEs against the measured WSEs, together with the corresponding SAR-estimated RIAs plotted against the measured WSEs. The RIA–WSE rating curve and the 1:1 line are also shown in Figure 8.

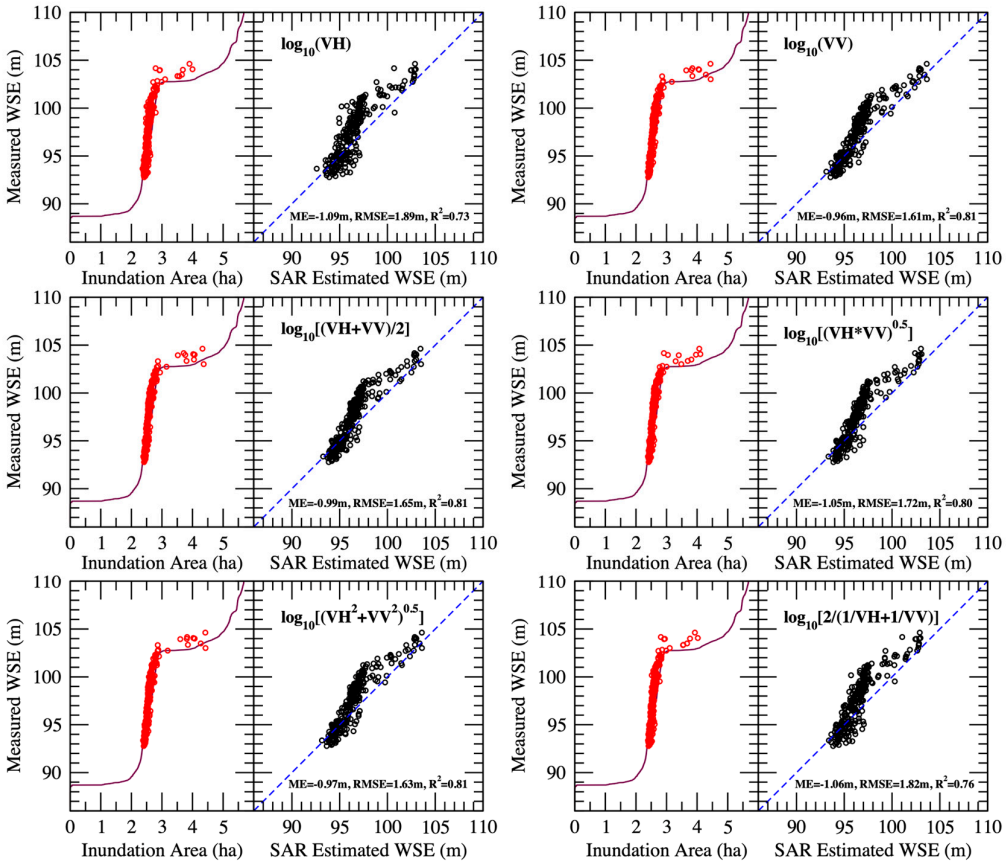


Figure 8. Relationships between SAR-estimated RIA and measured WSE, and between SAR-estimated and measured WSE, for the six SAR backscatter metrics. Red circles represent SAR-estimated RIAs and their corresponding measured WSEs, while black circles represent SAR-estimated WSEs plotted against measured WSEs. The purple solid line represents the TEM-derived RIA–WSE rating curve, and the blue dashed line represents the 1:1 line.

As illustrated in Figure 8, WSE estimates derived from $\log_{10}$(VH) and $\log_{10}$[2/(1/VH + 1/VV)] generally exhibit larger overall errors than those derived from the other four backscatter metrics, as reflected by their relatively higher RMSEs. However, their PLE values are not the lowest among the six metrics, indicating that these metrics can still provide the lowest absolute WSE error for a substantial number of individual SAR acquisitions. Despite differences in overall performance among the six metrics, they exhibit similar error characteristics across the range of measured WSEs. The estimated WSEs generally show a tendency toward underestimation, as indicated by the negative

MEs reported in Table 2. In addition, estimation errors are generally smaller when the measured WSE is below approximately 97.0 m or above approximately 102.5 m, whereas larger errors occur primarily within the intermediate WSE range of approximately 97.0–102.5 m.

The results in Figure 8 also indicate that the performance of an individual backscatter metric varies among SAR images. Therefore, rather than relying on a single metric for all observations, the six WSE estimates were further compared on an image-by-image basis. For each of the 265 SAR images, the estimate with the lowest absolute WSE error was identified. When two or more backscatter metrics produced the same lowest absolute WSE error, the metric with the higher overall PLE was selected. Based on the PLE values reported in Table 2, the priority order for resolving such ties was $\log_{10}(VV)$, $\log_{10}(VH)$, $\log_{10}[(VH^2 + VV^2)^{0.5}]$, $\log_{10}[2/(1/VH + 1/VV)]$, $\log_{10}[(VH \times VV)^{0.5}]$, and $\log_{10}[(VH + VV)/2]$. Figure 9 shows the best SAR-estimated WSEs and their corresponding RIAs selected from the six backscatter metrics using this procedure. Of the 265 selected estimates, 118 were obtained from $\log_{10}(VV)$, 70 from $\log_{10}(VH)$, 22 from $\log_{10}[(VH \times VV)^{0.5}]$, 21 from $\log_{10}[(VH^2 + VV^2)^{0.5}]$, 21 from $\log_{10}[2/(1/VH + 1/VV)]$, and 13 from $\log_{10}[(VH + VV)/2]$. Thus, although $\log_{10}(VV)$ provided the best estimate most frequently, accounting for 44.5% of the 265 SAR images, the other backscatter metrics produced the lowest absolute WSE error for a substantial number of images. These results indicate that no single backscatter metric consistently provides the most accurate WSE estimate across all SAR observations.

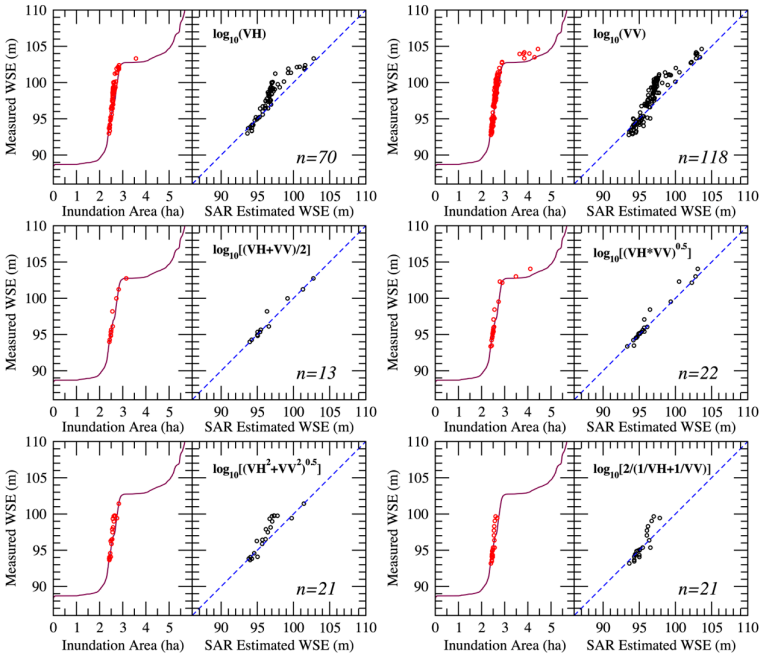


Figure 9. Best SAR-estimated WSEs and corresponding RIAs selected from the six SAR backscatter metrics. For each of the 265 SAR images, the estimate with the lowest absolute WSE error was selected; when multiple metrics produced the same lowest absolute error, the metric with the higher overall PLE was selected. *n* indicates the number of WSE estimates selected from each backscatter metric. The blue dashed line represents the 1:1 line.

Like Figures 8 and 9 shows that the SAR-estimated WSEs generally have smaller errors when the measured WSE is below 97.0 m or above 102.5 m, whereas larger errors occur primarily when the measured WSE is between 97.0 and 102.5 m. A WSE of 102.5 m represents the bankfull condition, corresponding to a bankfull depth of approximately 13.5 m given a channel-bed elevation of about 89.0 m. A WSE of 97.0 m corresponds to a

water depth of approximately 8.0 m, or about 59% of the bankfull depth. Accordingly, three flow conditions are defined in this study: low-flow conditions, with WSE below 97.0 m (water depth < 59% of the bankfull depth); medium- to high-flow conditions, with WSE between 97.0 and 102.5 m; and flooding conditions, with WSE above 102.5 m. In the following subsections, the error characteristics of the SAR-estimated WSEs are evaluated under these three flow conditions to investigate the effects of riverbank vegetation, wind and waves, and river morphology, with particular emphasis on identifying the conditions under which each of the six backscatter metrics is most effective for extracting river inundation areas from SAR imagery.

5.2. Effect of Riverbank Vegetation on SAR-Estimated WSEs

To investigate the effects of riverbank vegetation on SAR-estimated WSEs, 10 NAIP images acquired from 2015 to 2024 were used to calculate the normalized difference vegetation index (NDVI). The USDA NAIP is specifically designed to acquire "leaf-on" aerial imagery during the peak growing season. Consequently, the available NAIP images represent growing-season vegetation conditions, when vegetation greenness and leaf cover are generally greatest and their potential interference with SAR-based water detection may be more pronounced than during winter. The NDVI analysis was used to assess the potential influence of vegetation on SAR-derived inundation areas rather than to guide SAR water detection. The analysis was conducted within the same predefined polygon used for extracting RIAs from the Sentinel-1 SAR images and subsequently estimating WSEs. The mean and standard deviation of NDVI were then calculated along WSE contour lines from 95.0 to 105.0 m at 1.0-m intervals within the polygon. The resulting mean NDVI values and corresponding standard deviations are presented in Figure 10.

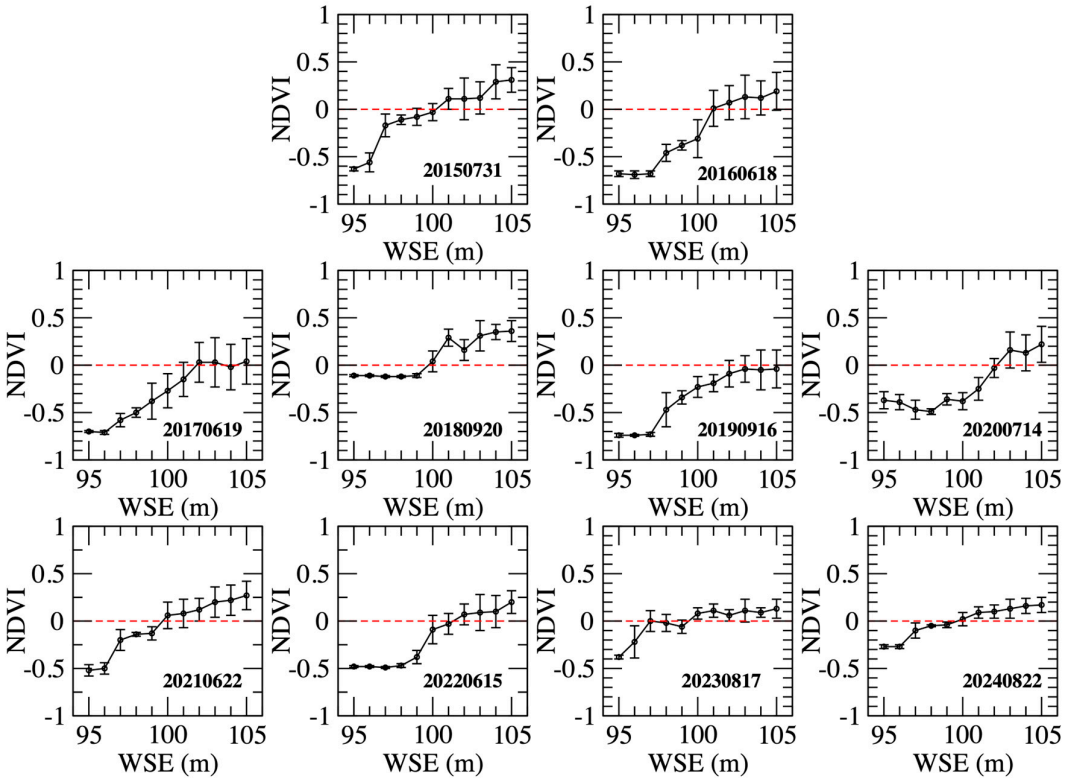


Figure 10. Mean and standard deviation of NDVI along WSE contour lines from 95.0 to 105.0 m derived from NAIP imagery acquired during 2015–2024. Error bars represent ± standard deviation. The red dashed line represents NDVI = 0.

As shown in Figure 10, mean NDVI generally increases with WSE. When WSE is below approximately 100.0 m, mean NDVI is predominantly negative or close to zero across the 10 NAIP images, indicating limited vegetation along the corresponding WSE contours. Thus, under low-flow conditions (WSE < 97.0 m), vegetation is unlikely to be a major factor affecting the extraction of river inundation boundaries from SAR imagery. Under medium- to high-flow conditions (97.0–102.5 m), however, the potential influence of vegetation increases as the water level rises along the riverbanks. This influence becomes more evident when WSE exceeds approximately 100.0 m, where mean NDVI generally approaches or becomes greater than zero, indicating increasing vegetation along the inundation boundary. Vegetation may therefore contribute to the larger WSE estimation errors observed under medium- to high-flow conditions, particularly at WSEs above 100.0 m. However, the variation in WSE estimation errors among the three flow conditions cannot be attributed to vegetation alone. Wind-generated waves and river morphology may also affect SAR backscatter and the detection of the water–land boundary, and their effects may vary with flow conditions. The combined effects of these factors are further examined in the following subsection.

5.3. Effects of Wind, Waves, and River Morphology on SAR-Estimated WSEs

In addition to vegetation, wind-generated water surface roughness and river morphology may contribute to errors in SAR-derived RIAs and WSEs. The overall underestimation of WSE observed in this study may be partly attributed to two mechanisms that produce relatively strong SAR backscatter near the water–land boundary. First, vegetation along the riverbanks may produce relatively strong SAR backscatter from leaves, branches, and trunks, making the underlying or adjacent water surfaces difficult to distinguish from non-water areas and potentially causing underestimation of the SAR-derived RIA. Second, wind-induced water surface roughness near the water-land boundary can increase SAR backscatter and cause portions of the water surface to be misclassified as non-water. Both mechanisms can lead to underestimation of the SAR-derived RIA and, consequently, the corresponding WSE. River morphology may further influence WSE estimation because riverbank and floodplain slopes determine how errors in the horizontal position of the delineated water–land boundary translate into WSE errors. River morphology also affects wind-wave development by controlling effective fetch, water depth, and sheltering by the riverbanks.

SAR backscatter is strongly influenced by surface roughness relative to the radar wavelength and by imaging geometry. Riverbanks covered by dense vegetation generally produce relatively strong and spatially heterogeneous backscatter because of scattering from leaves, branches, stems, and canopy structure. Even sparsely vegetated or bare riverbanks can produce moderate to strong backscatter when surface roughness occurs at scales relevant to the radar wavelength. Sentinel-1 operates in the C-band with a wavelength of approximately 5.6 cm and is therefore sensitive to centimeter-scale surface roughness. In contrast, calm and smooth water surfaces generally produce low backscatter because most of the incident radar energy is reflected away from the sensor.

Various types of surface waves can occur on rivers [75,76], including capillary waves, wind-generated gravity waves, standing waves, flood waves, and roll waves. For C-band SAR observations, the wavelengths of larger-scale waves do not necessarily correspond directly to the roughness scales sensed by the radar. Rather, wind-generated waves can modify the spectrum of small-scale surface roughness, including centimeter-scale

capillary and short gravity waves that contribute strongly to radar backscatter. Consequently, a river surface affected by wind and waves can exhibit substantially greater backscatter than a calm water surface, making discrimination between water and adjacent land more difficult.

The development of wind-generated water surface roughness depends on both wind speed and the effective fetch over which the wind acts on the water surface. As wind speed and effective fetch increase, wave development and small-scale surface roughness generally increase, resulting in stronger and more spatially variable SAR backscatter [77]. Under calm or sheltered conditions, the water surface tends to remain relatively smooth and produces low SAR backscatter, facilitating discrimination between water and non-water pixels. Wind direction is also important because effective fetch depends on the orientation of the wind relative to the river channel. Winds blowing approximately along the river channel may have a longer effective fetch than winds blowing across the channel and may therefore favor greater wave development under otherwise similar wind speeds. However, this effect also depends on local channel geometry, surrounding terrain, vegetation, and water depth.

To evaluate the impact of wind direction and speed on the accuracy of the SAR-estimated WSEs, five-minute Automated Surface Observing System (ASOS) observations from the Cape Girardeau FAA Airport (KCGI), located approximately 10 km west of the USGS gauging station at Thebes, were used. Wind observations corresponding to the acquisition times of the 265 SAR images were extracted from the ASOS dataset. Wind direction observations were available for 244 acquisitions, whereas wind speed observations were available for 245 acquisitions. Wind direction follows the standard meteorological convention, indicating the direction from which the wind originates and measured clockwise from north. Wind directions were grouped into eight 45° sectors: N (337.5–22.5°), NE (22.5–67.5°), E (67.5–112.5°), SE (112.5–157.5°), S (157.5–202.5°), SW (202.5–247.5°), W (247.5–292.5°), and NW (292.5–337.5°). Wind speeds were classified according to the Beaufort wind force scale [78]. Among the SAR acquisitions with available wind speed observations, wind speeds ranged from calm conditions to a maximum of 25 kt, corresponding to Beaufort Numbers (BNs) 0–6. The wind speed ranges and corresponding wind conditions for BNs 0–6 are summarized in Table 3. Scatter plots of SAR-estimated versus measured WSEs for the six backscatter metrics under different wind directions (WDs) and wind speeds (WSs) are shown in Figure 11.

Table 3. Description of wind conditions corresponding to Beaufort numbers 0–6, used for categorizing wind conditions during the 265 SAR acquisitions in this study.

BN	0	1	2	3	4	5	6
Wind speed (kt)	<1	1–3	4–6	7–10	11–16	17–21	22–27
Description	Calm	Light air	Light breeze	Gentle breeze	Moderate breeze	Fresh breeze	Strong breeze

Northerly and southerly winds were the most frequently observed wind directions, accounting for 68 (27.9%) and 67 (27.5%) acquisitions, respectively, while wind speeds were dominated by BN2 and BN3, which together accounted for 67.8% of the observations. Visual inspection of Figure 11 suggests that the effects of wind speed on WSE estimation errors vary with flow conditions. Under low-flow conditions (WSE < 97.0 m), estimation errors are generally small across the observed wind-speed classes. Under medium- to high-flow conditions (97.0–102.5 m), however, BN3 observations (7–10 kt) frequently exhibit larger deviations from the 1:1 line than observations associated with the lower wind-speed classes (BN0–BN2) across several backscatter metrics. Under flooding conditions (WSE > 102.5 m), estimation errors generally decrease again despite the occurrence of moderate wind speeds. These patterns suggest that the influence of wind

speed on SAR-estimated WSE may be flow-dependent rather than uniform across different water levels. In contrast, no consistent relationship between WSE estimation error and wind direction is apparent from Figure 11 across the six backscatter metrics.

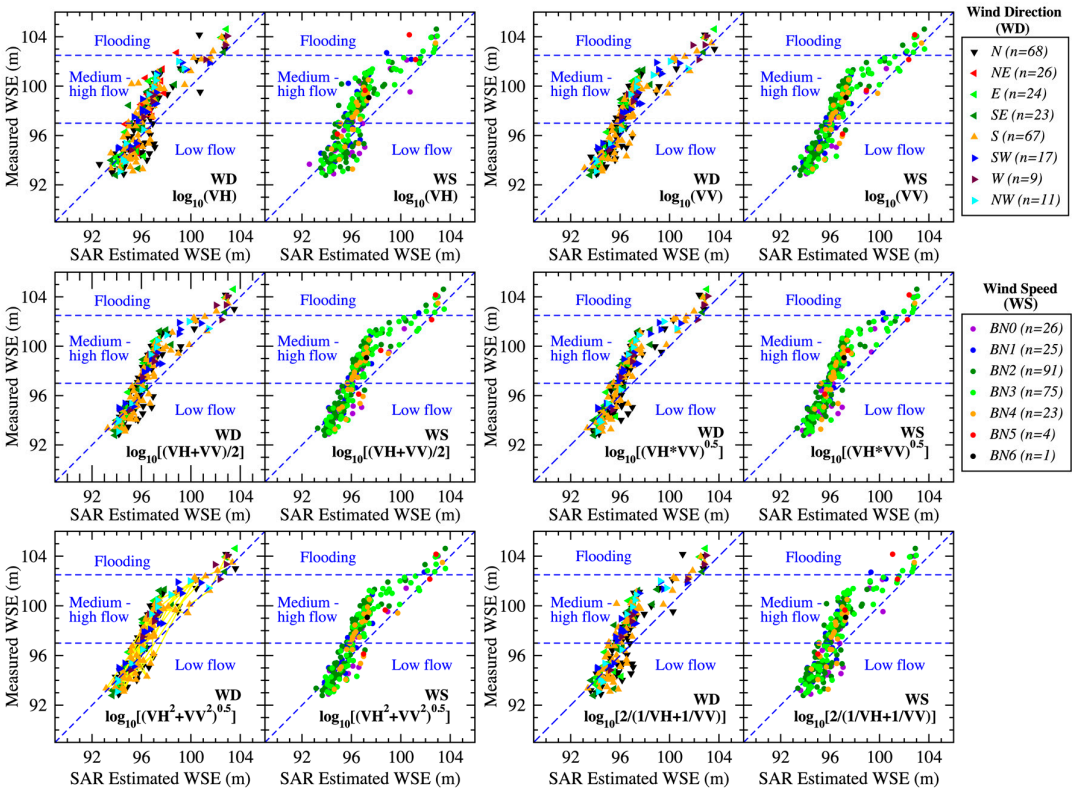


Figure 11. Relationships between SAR-estimated and measured WSEs for the six backscatter metrics under different wind directions (WDs) and wind speeds (WSs). Wind speeds are classified using Beaufort Numbers (BNs). The horizontal dashed lines indicate the WSE thresholds separating low-flow (WSE < 97.0 m), medium- to high-flow (97.0–102.5 m), and flooding (WSE > 102.5 m) conditions. The blue dashed line represents the 1:1 line.

To quantitatively evaluate the apparent effects of wind speed and wind direction, the mean error (ME) and mean absolute error (MAE) of the SAR-estimated WSEs was further calculated for different wind conditions under each of the three flow regimes. To increase the sample size within individual wind categories, BN5 and BN6 were combined into a single BN5–6 class because only five observations occurred within these two wind-speed classes. Similarly, the eight wind-direction sectors were combined into four wind-orientation groups consisting of opposite directions: N–S, NE–SW, E–W, and SE–NW. This grouping also facilitates evaluation of wind orientation relative to the generally north–south-oriented river channel, particularly the contrast between approximately along-channel (N–S) and cross-channel (E–W) winds. The ME, MAE, and corresponding sample size (n) were then calculated for each wind-orientation group and wind-speed class under the three flow regimes and for each of the six backscatter metrics, as summarized in Tables 4 and 5, respectively.

Table 4. Summary of the ME and MAE of the six backscatter metrics for the four wind-orientation groups under the three flow regimes.

		$\log_{10}$(VH)		$\log_{10}$(VV)		$\log_{10}$[(VH + VV)/2]		$\log_{10}$[(VH ∗ VV)$^{0.5}$]		$\log_{10}$[(VH^2 + VV^2)$^{0.5}$]		$\log_{10}$[2/(1/VH + 1/VV)]	
		ME (m)	**MAE (m)**	**ME (m)**	**MAE (m)**	**ME (m)**	**MAE (m)**	**ME (m)**	**MAE (m)**	**ME (m)**	**MAE (m)**	**ME (m)**	**MAE (m)**
Low flow	N–S (*n* = 65)	0.39	0.91	0.32	0.74	0.33	0.71	0.32	0.71	0.33	0.74	0.39	0.84
	NE–SW (*n* = 12)	−0.05	0.65	−0.15	0.55	−0.12	0.57	−0.07	0.58	−0.13	0.54	0.00	0.63
	E–W (*n* = 13)	0.00	0.66	0.04	0.48	0.04	0.47	0.03	0.55	0.04	0.48	−0.01	0.66
	SE–NW (*n* = 16)	0.21	0.83	0.01	0.47	0.03	0.52	0.06	0.65	0.00	0.47	0.15	0.75
Medium-high flow	N–S (*n* = 64)	−2.09	2.13	−1.85	1.88	−1.92	1.92	−2.01	2.01	−1.87	1.89	−2.06	2.09
	NE–SW (*n* = 30)	−2.10	2.10	−1.84	1.84	−1.92	1.92	−2.00	2.00	−1.87	1.87	−2.07	2.07
	E–W (*n* = 15)	−2.35	2.35	−2.23	2.26	−2.25	2.29	−2.28	2.30	−2.24	2.27	−2.34	2.34
	SE–NW (*n* = 17)	−2.57	2.57	−2.22	2.23	−2.31	2.32	−2.44	2.44	−2.27	2.27	−2.51	2.51
Flooding	N–S (*n* = 6)	−1.35	1.35	−0.58	0.79	−0.70	0.87	−0.97	0.97	−0.60	0.80	−1.27	1.27
	NE–SW (*n* = 1)	−3.86	3.86	−0.59	0.59	−1.25	1.25	−2.43	2.43	−0.81	0.81	−3.39	3.39
	E–W (*n* = 5)	−1.08	1.08	−1.02	1.02	−1.04	1.04	−0.97	0.97	−1.02	1.02	−1.08	1.08
	SE–NW (*n* = 1)	−0.10	0.10	0.02	0.02	0.01	0.01	−0.08	0.08	0.02	0.02	−0.10	0.10

Table 4 summarizes the ME and MAE of the six backscatter metrics for the four wind-orientation groups under the three flow regimes. Under low-flow conditions, MEs were generally close to zero and MAEs were relatively small across all wind-orientation groups, with no consistent relationship between wind orientation and WSE estimation error. Under medium- to high-flow conditions, all six backscatter metrics exhibited negative MEs for each wind-orientation group, indicating systematic WSE underestimation. The E–W and SE–NW groups generally exhibited larger MAEs than the N–S and NE–SW groups. For example, for $\log_{10}$(VV), the MAEs were 1.88 and 1.84 m for the N–S and NE–SW groups, respectively, compared with 2.26 and 2.23 m for the E–W and SE–NW groups. The consistency of this pattern across the six backscatter metrics suggests that wind orientation relative to the river channel may influence WSE estimation errors under medium- to high-flow conditions.

Although winds approximately aligned with the generally north–south-oriented river channel may provide a longer effective fetch for wave development, the larger errors associated with the E–W and SE–NW groups indicate that effective fetch alone cannot explain the observed directional pattern. Winds with a stronger cross-channel component may affect near-bank water-surface conditions differently from winds oriented approximately along the channel. Depending on wind direction, wind-generated waves may propagate either toward or away from the riverbank along which the water–land boundary used to derive RIA and WSE is delineated. When waves propagate toward this riverbank, shoaling, wave breaking, and associated turbulence may enhance small-scale water surface roughness near the water–land boundary. In contrast, when waves propagate away from the riverbank, different near-bank surface conditions may develop. These directional differences in near-bank water surface roughness could affect SAR backscatter and water–land boundary delineation, thereby contributing to differences in RIA and WSE estimation errors among the wind-orientation groups. To further examine how wind orientation affects the most accurate WSE estimates obtained from the six backscatter metrics, the best SAR-estimated WSE for each acquisition was grouped according to the four wind-orientation groups and is presented in Figure 12.

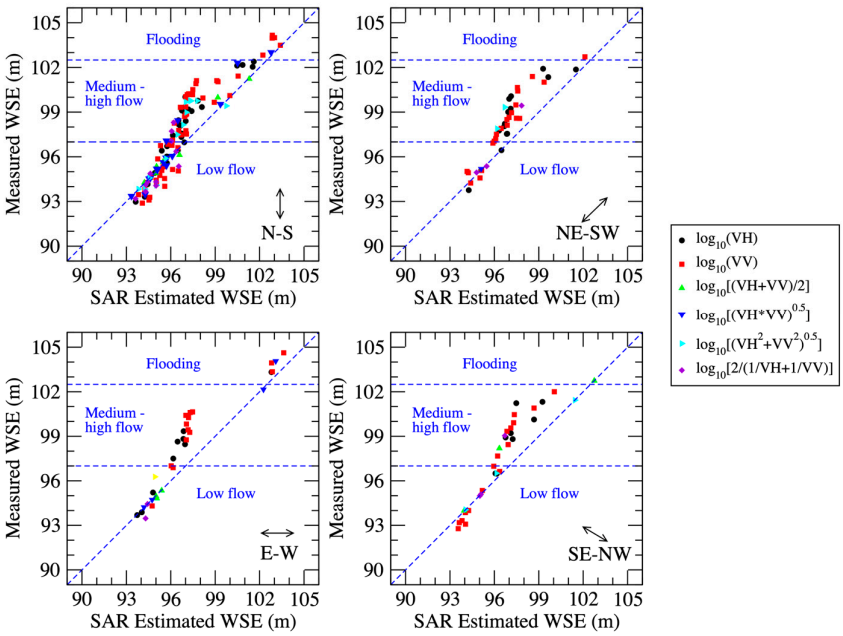


Figure 12. Best SAR-estimated WSEs selected from the six backscatter metrics under four wind-orientation groups. The blue dashed line represents the 1:1 line.

According to Figure 12, under low-flow conditions, the WSE estimates generally lie close to the 1:1 line regardless of wind orientation. Several N–S observations below approximately 96 m show slight overestimation, similar to that observed in the independent NAIP validation (Figure 3), suggesting that uncertainty in the low-WSE portion of the RIA–WSE relationship may partly contribute to these errors. Under medium- to high-flow conditions, systematic WSE underestimation is evident, particularly for the E–W and SE–NW groups, consistent with their larger MAEs in Table 4. Although winds approximately aligned with the generally north–south-oriented river channel may provide longer effective fetch, the larger errors for E–W and SE–NW winds indicate that effective fetch alone cannot explain the directional differences. Winds with stronger cross-channel components may produce different near-bank surface-roughness conditions and wave–bank interactions, thereby affecting SAR backscatter and water–land boundary delineation.

Under flooding conditions, the WSE estimates generally show smaller departures from the 1:1 line than under medium- to high-flow conditions. However, the small number of flooding observations prevents reliable evaluation of wind-orientation effects. Overall, the results indicate that wind-orientation effects are flow-dependent and are most evident under medium- to high-flow conditions. Because wave characteristics and near-bank water surface roughness were not directly measured, the proposed effects of wind orientation and wave–bank interactions should be regarded as physically based interpretations rather than directly verified mechanisms.

Table 5 summarizes the ME and MAE of the six backscatter metrics across wind-speed classes under the three flow regimes. Under low-flow conditions, errors were relatively small, with no consistent increase with wind speed. Under medium- to high-flow conditions, MEs were consistently negative, indicating systematic WSE underestimation, and BN0 generally had smaller MAEs than BN1–BN4 across all six metrics. For example, the MAE of $\log_{10}$(VV) was 1.47 m for BN0, compared with 2.11, 2.21, 1.88, and 1.73 m for BN1–BN4, respectively. This suggests that wind-generated water surface roughness may increase WSE estimation errors, although the absence of a

monotonic increase from BN1 to BN4 indicates that errors are more strongly associated with the transition from calm to non-calm conditions than with increasing wind speed. Under flooding conditions, errors were generally smaller than under medium- to high-flow conditions, but the small sample sizes, particularly for BN5–6, limit interpretation of wind-speed effects.

Table 5. Mean error (ME) and mean absolute error (MAE) of SAR-estimated WSEs for the six backscatter metrics under different wind-speed classes and flow regimes.

		$\log_{10}$(VH)		$\log_{10}$(VV)		$\log_{10}$[(VH + VV)/2]		$\log_{10}$[(VH ∗ VV)$^{0.5}$]		$\log_{10}$[(VH^2 + VV^2)$^{0.5}$]		$\log_{10}$[2/(1/VH + 1/VV)]	
		ME (m)	**MAE (m)**	**ME (m)**	**MAE (m)**	**ME (m)**	**MAE (m)**	**ME (m)**	**MAE (m)**	**ME (m)**	**MAE (m)**	**ME (m)**	**MAE (m)**
Low flow	BN0 (n = 16)	0.43	0.90	0.30	0.72	0.36	0.78	0.43	0.83	0.32	0.74	0.50	0.85
	BN1 (n = 13)	−0.02	0.80	−0.23	0.51	−0.19	0.47	−0.15	0.47	−0.21	0.49	−0.03	0.68
	BN2 (n = 39)	0.28	0.88	0.05	0.49	0.09	0.52	0.16	0.62	0.06	0.50	0.26	0.80
	BN3 (n = 28)	0.36	0.70	0.43	0.79	0.40	0.71	0.33	0.66	0.43	0.78	0.34	0.68
	BN4 (n = 9)	0.17	1.03	0.35	0.86	0.33	0.90	0.17	0.92	0.35	0.87	0.15	1.02
	BN5–6 (n = 1)	−1.27	1.27	0.89	0.89	0.46	0.46	−0.55	0.55	0.86	0.86	−1.11	1.11
Medium-high flow	BN0 (n = 9)	−1.50	1.78	−1.47	1.47	−1.51	1.51	−159	1.59	−1.48	1.48	−1.55	1.71
	BN1 (n = 11)	−2.46	2.46	−2.11	2.11	−2.17	2.17	−2.27	2.27	−2.12	2.12	−2.36	2.36
	BN2 (n = 49)	−2.28	2.28	−2.21	2.21	−2.24	2.24	−2.25	2.25	−2.23	2.23	−2.26	2.26
	BN3 (n = 41)	−2.28	2.38	−1.86	1.88	−1.95	1.96	−2.09	2.09	−1.90	1.92	−2.22	2.22
	BN4 (n = 13)	−1.92	1.92	−1.66	1.73	−1.79	1.79	−1.94	1.94	−1.69	1.75	−1.94	1.94
	BN5–6 (n = 3)	−1.72	1.72	−0.76	0.91	−0.93	1.16	−1.35	1.42	−0.83	0.97	−1.65	1.65
Flooding	BN0 (n = 1)	−1.18	1.18	−0.98	0.98	−0.98	0.98	−1.08	1.08	−0.98	0.98	−1.16	1.16
	BN1 (n = 1)	−3.86	3.86	−0.59	0.59	−1.25	1.25	−2.43	2.43	−0.81	0.81	−3.39	3.39
	BN2 (n = 3)	−1.24	1.24	−1.18	1.18	−1.19	1.19	−1.14	1.14	−1.17	1.17	−1.23	1.23
	BN3 (n = 6)	−0.76	0.76	−0.44	0.66	−0.50	0.67	−0.64	0.64	−0.46	0.67	-0.75	0.75
	BN4 (n = 1)	−0.68	0.68	−0.10	0.10	−0.50	0.50	-0.65	0.65	−0.12	0.12	−0.68	0.68
	BN5–6 (n = 1)	−3.47	3.47	−1.30	1.30	−1.34	1.34	−1.76	1.76	−1.31	1.31	−3.10	3.10

To further examine the differences in the best SAR-estimated WSEs between calm and non-calm conditions, the best WSE estimate for each acquisition was grouped according to wind-speed class and is presented in Figure 13. Because of the very small number of observations in BN5–6, only BN0–BN4 are shown. Different symbols and colors indicate the backscatter metric from which each best WSE estimate was obtained.

Figure 13 further illustrates the flow-dependent effects of wind speed on the best SAR-estimated WSEs. Under low-flow conditions, estimates generally lie close to the 1:1 line across BN0–BN4. Under medium- to high-flow conditions, BN0 estimates are generally closer to the 1:1 line, whereas greater underestimation occurs under BN1–BN4, consistent with Table 5. However, the departures from the 1:1 line do not progressively increase from BN1 to BN4, confirming the absence of a monotonic relationship between wind speed and WSE error. Under flooding conditions, the limited observations prevent a robust comparison among wind-speed classes.

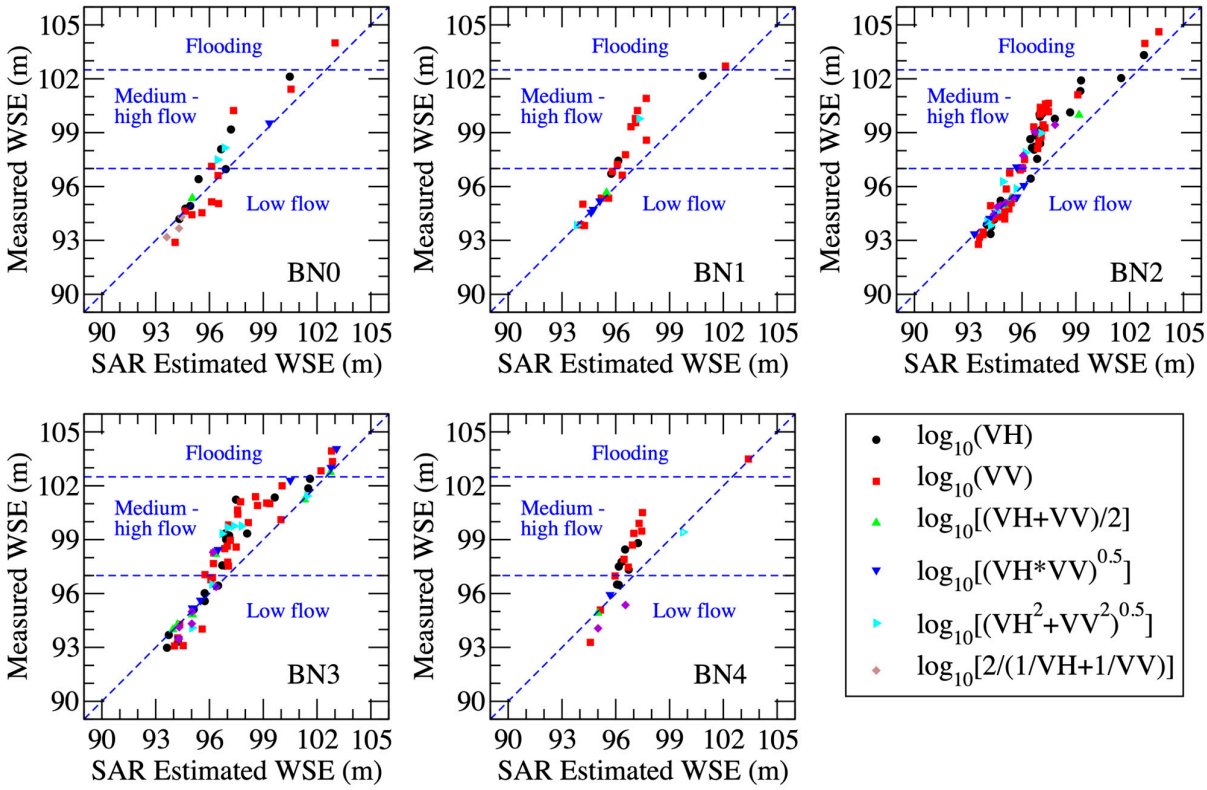


Figure 13. Best SAR-estimated WSEs selected from the six backscatter metrics under different wind-speed classes (BN0–BN4). The blue dashed line represents the 1:1 line.

5.4. Limitations

Several limitations of this study should be acknowledged. First, the analysis was conducted at a single reach of the Mississippi River near the Thebes gauging station. Therefore, the performance of the proposed RIA–WSE approach and the effects of vegetation, wind, waves, and river morphology may differ for rivers with different channel widths, bank and floodplain slopes, vegetation characteristics, and hydrologic regimes. Second, wind observations were obtained from the nearest ASOS station, located approximately 10 km from the study site and about 10 m higher in elevation than the gauging station, and may not fully represent local wind conditions over the river because of spatial heterogeneity in wind speed and direction. Moreover, no direct measurements of wave characteristics or water-surface roughness were available. Consequently, the inferred effects of wind-generated waves, effective fetch, and wave–bank interactions on SAR backscatter and WSE estimation should be regarded as physically based interpretations rather than directly observed mechanisms. Third, vegetation conditions were characterized using NDVIs derived from 10 NAIP images during the growing seasons of 2015–2024, whereas vegetation conditions at the time of individual Sentinel-1 acquisitions may differ because of seasonal and short-term variations.

Although the Sentinel-1 SAR data were resampled from 10-m to 1-m pixel spacing to facilitate water–land boundary delineation and integration with the high-resolution topobathymetric elevation data, resampling does not increase the intrinsic spatial information contained in the original SAR observations. The sensitivity analysis (Section 4.3) showed that finer grid spacing did not consistently improve WSE estimation accuracy and threshold selection had a greater influence on the performance of some backscatter metrics, particularly $\log_{10}$(VH) and the harmonic-mean metric. Consequently,

uncertainties associated with mixed water–land pixels and complex or vegetated shorelines remain. In addition, the accuracy of WSE estimates depends on the constructed RIA–WSE relationship and, consequently, on the accuracy and spatial resolution of the topobathymetric elevation model. The broader applicability of the proposed approach may therefore be limited in river reaches where sufficiently accurate and high-resolution topographic or topobathymetric elevation data are unavailable. The NAIP validation and SAR results suggest that some uncertainty may exist in the RIA–WSE relationship at very low WSEs, which may partly contribute to the observed WSE estimation errors under low-flow conditions.

Finally, although the 265 SAR acquisitions provide a substantial dataset for evaluating overall WSE estimation performance, sample sizes become considerably smaller when the observations are subdivided by flow regime, wind speed, wind orientation, and other environmental conditions. This limitation is particularly evident for flooding conditions and the higher wind-speed classes, for which only a small number of observations were available. The available dataset is therefore insufficient to establish robust condition-specific criteria for selecting among the six backscatter metrics or to fully separate the individual and combined effects of wind, vegetation, river morphology, and hydrologic conditions. Future studies incorporating in situ wind and wave observations, acquisition-date vegetation information, higher-resolution SAR observations, and additional river reaches with contrasting morphologic and hydrologic characteristics would help further evaluate the mechanisms identified in this study, assess the transferability of the proposed method, and support the development and validation of condition-dependent approaches for selecting SAR backscatter metrics for WSE estimation.

6. Conclusions

This study developed and evaluated a Sentinel-1 SAR-based approach for estimating river WSE using a river inundation area–water surface elevation (RIA–WSE) relationship constructed from U.S. Geological Survey Topobathymetric Elevation Model (TEM) data. A total of 265 Sentinel-1 images acquired during 2015–2026 at the Thebes gauging station along the Mississippi River were analyzed using six VV- and VH-based backscatter metrics, yielding 1590 WSE estimates. Among the six metrics, $\log_{10}$(VV) provided the best overall performance, with an RMSE of 1.61 m, ME of −0.96 m, R^2 of 0.81, and PLE of 44.5%.

Comparison of the TEM-derived and conventional DEM-derived RIA–WSE relationships highlighted the importance of incorporating submerged channel bathymetry for estimating WSE at low river stages. The SAR image grid-spacing sensitivity analysis further showed that $\log_{10}$(VV) maintained relatively low and stable estimation errors across grid spacings of 10, 5, 2, and 1 m, whereas finer resampling did not consistently improve WSE estimation accuracy. These findings emphasize the importance of DEM characteristics and threshold selection in SAR-based WSE retrieval.

The results demonstrate that the accuracy of SAR-derived WSE varies substantially with flow condition and is influenced by the combined effects of vegetation, wind-generated water surface roughness, and river morphology. WSE estimation errors were smallest under low-flow conditions (WSE < 97.0 m), largest under medium- to high-flow conditions (97.0–102.5 m) and decreased again under flooding conditions (WSE > 102.5 m). Analysis of 10 NAIP images showed increasing vegetation along the inundation boundary at WSEs above approximately 100 m, suggesting increasing vegetation effects on water–land boundary delineation as river stage rises. Riverbank and floodplain morphology also affect how errors in the horizontal position of the detected inundation boundary translate into WSE uncertainty, with steep riverbanks increasing this sensitivity and gently sloping floodplains reducing it.

The wind analysis further showed that the effects of wind on WSE estimation depend strongly on flow condition. Under low-flow conditions, errors remained relatively small across the observed wind-speed classes. Under medium- to high-flow conditions, however, calm conditions (BN0) generally produced smaller MAEs than non-calm conditions (BN1–BN4) across all six backscatter metrics, indicating that the presence of wind may contribute to increased WSE estimation errors through wind-generated water surface roughness. Nevertheless, errors did not increase monotonically with wind speed, suggesting that the transition from calm to non-calm conditions is more clearly associated with increased error than differences in wind speed among non-calm conditions. Wind orientation also affected estimation accuracy under medium- to high-flow conditions, with the E–W and SE–NW orientation groups generally exhibiting larger MAEs than the N–S and NE–SW groups. These results indicate that wind effects cannot be explained by wind speed or effective fetch alone and may also depend on wind orientation relative to the river channel and resulting near-bank water surface conditions.

Although $\log_{10}$(VV) provided the best overall performance, it produced the lowest absolute WSE error for only 44.5% of the 265 SAR acquisitions, indicating that other backscatter metrics could outperform $\log_{10}$(VV) under certain environmental and hydrologic conditions. These findings suggest that no single backscatter metric is optimal under all environmental and hydrologic conditions and highlight the potential of condition-dependent retrieval approaches that consider flow regime, vegetation, wind speed and orientation, effective fetch, and river morphology.

Overall, this study demonstrates the potential of Sentinel-1 SAR for long-term river WSE monitoring while highlighting the importance of environmental and geomorphic controls on retrieval accuracy. Future studies incorporating these controls and encompassing rivers with diverse channel and hydrologic characteristics could support the development and validation of more robust and transferable condition-dependent approaches for SAR-based river WSE estimation, complementing other satellite-based water-level monitoring capabilities.

Funding: This research received no external funding.

Data Availability Statement: The original datasets used in this study are publicly available from the data providers cited in the manuscript. River stage data were obtained from the U.S. Geological Survey (USGS) Water Data for the Nation (WDFN) database, NAIP images were downloaded from USGS EarthExplorer, SAR images were obtained from the Alaska Satellite Facility (ASF), 5-min wind speed and direction data were obtained from NOAA Automated Surface Observing Systems (ASOS) network. The processed datasets generated and analyzed during this study are available from the corresponding author upon reasonable request.

Acknowledgments: Thanks to the Upper Midwest Environmental Science Center (UMESC) for producing the topobaythmetric elevation (TEM) data along the Upper Mississippi River and making the TEM data available to public, the European Space Agency (ESA) for developing the ESA Sentinel Application Platform (SNAP) and making it public available, and four anonymous referees for their useful comments and suggestions. ChatGPT (GPT-6, OpenAI) was used for limited language assistance, specifically for grammar correction and sentence polishing to improve clarity and readability. The author reviewed and edited all AI-assisted output and takes full responsibility for the content, scientific accuracy, and integrity of this publication.

Conflicts of Interest: The author declares no conflicts of interest.

References

1. Buchanan, T.J.; Somers, W.P. Discharge measurements at gaging stations. In *Techniques for Water Resources Investigation of the United States Geological Survey*; Book 3; U.S. Geological Survey: Reston, VA, USA, 1969; Volume A8.
2. Olson, S.A.; Norris, J.M. *U.S. Geological Survey Streamgaging*; Fact Sheet; U.S. Geological Survey: Reston, VA, USA, 2007.
3. Hamed, K.; Rao, A.R. *Flood Frequency Analysis*, 1st Ed.; CRC Press: Boca Raton, FL, USA, 2000; p. 376.
4. Bhat, M.S.; Alam, A.; Ahmad, B.; Katlia, B.S.; Farooq, H.; Taloor, A.K.; Ahmad, S. Flood frequency analysis of river Jhelum in Kashmir Basin. *Quat. Int.* **2019**, *507*, 288–294.
5. Faulkner, D.; Warren, S.; Spencer, P.; Sharkey, P. Can we still predict the future from the past? Implementing non-stationary flood frequency analysis in the UK. *J. Flood Risk Manag.* **2019**, *13*, e12582.
6. Bischiniotis, K.; de Moel, H.; van den Homberg, M.; Couasnon, A.; Aerts, J.; Nobre, G.G.; Zsoter, E.; van den Hurk, B. A framework for comparing permanent and forecast-based flood risk-reduction strategies. *Sci. Total Environ.* **2020**, *720*, 137572.
7. Speight, L.J.; Cranston, M.D.; White, C.J.; Kelly, L. Operational and emerging capabilities for surface water flood forecasting. *Wiley Interdiscip. Rev. Water* **2021**, *8*, e1517.
8. Jain, S.K.; Singh, V.P. *Water Resources Systems Planning and Management*, 2nd Ed.; Elsevier: Amsterdam, The Netherlands, 2023; p. 893.
9. Niu, W.; Feng, Z. Evaluating the performances of several artificial intelligence methods in forecasting daily streamflow times series for sustainable water resources management. *Sustain. Cities Soc.* **2021**, *64*, 102562.
10. Abbott, B.W.; Bishop, K.; Zarnetske, J.P.; Minaudo, C.; Chapin, F.S.; Krause, S.; Hannah, D.M.; Conner, L.; Ellison, D.; Godsey, S.E.; et al. Human domination of the global water cycle absent from depictions and perceptions. *Nat. Geosci.* **2019**, *12*, 533–540.
11. Gleeson, T.; Wang-Erlandsson, L.; Porkka, M.; Zipper, S.C.; Jaramillo, F.; Gerten, D.; Fetzer, I.; Cornell, S.E.; Piemontese, L.; Gordon, L.J.; et al. Illumination water cycle modifications and earth system resilience in the Anthropocene. *Water Resour. Res.* **2020**, *56*, e2019WR024957.
12. Suwal, N.; Huang, X.; Kuriqi, A.; Chen, Y.; Pandey, K.P.; Bhattarai, K.P. Optimization for cascade reservoir operation considering environmental flows for different environmental management classes. *Renew. Energy* **2020**, *158*, 453–464.
13. Zhang, S.; Jing, Z.; Li, W.; Wang, L.; Liu, D.; Wang, T. Navigation risk assessment method based on flow conditions: A case study of the river reach between the Three Gorge Dam and the Gezhouba Dam. *Ocean Eng.* **2019**, *175*, 71–79.
14. Kwon, S.; Seo, I.; Kim, B.; Jung, S.; Kim, Y. Assessment of river recreation safety using spatial river recreational index by integration of hydrodynamic model and fuzzy logic. *Res. Sq.* **2023**, *in press*. https://doi.org/10.21203/rs.3.rs-2827493/v1.
15. Grizzetti, B.; Liquete, C.; Pistocchi, A.; Vigiak, O.; Zulian, G.; Bouraoui, F.; De Roo, A.; Cardoso, A.C. Relationship between ecological condition and ecosystem services in European rivers, lakes and coastal waters. *Sci. Total Environ.* **2019**, *671*, 452–465.
16. Fekete, B.M.; Vörösmarty, C.J. The current status of global river discharge monitoring and potential new technologies complementing traditional discharge measurements. In *Proceedings of the PUB Kick-Off Meeting, Brasilia, Brazil, 20–22 November 2002*; IAHS Publication: Wallingford, UK, 2007; p. 309.
17. Vörösmarty, C.J.; Willmott, C.J.; Choudhury, B.J.; Schloss, A.L.; Stearns, T.K.; Robeson, S.M.; Dorman, T.J. Analyzing the discharge regime of a large tropical river through remote sensing, ground-based climatic data and modeling. *Water Resour. Res.* **1996**, *32*, 3137–3150.
18. The Ad Hoc Group; Vörösmarty, C.; Askew, A.; Grabs, W.; Barry, R.G.; Birkett, C.; Döll, P.; Goodison, B.; Hall, A.; Jenne, R.; et al. Global Water Data: A newly endangered species. *EOS Trans. Am. Geophys. Union* **2001**, *82*, 54–58.
19. Bjerklie, D.M.; Dingman, S.L.; Vörösmarty, C.J.; Holster, C.H.; Congalton, R.G. Evaluating the potential for measuring river discharge from space. *J. Hydrol.* **2003**, *278*, 17–38.
20. Hannah, D.M.; Demuth, S.; van Lanen, H.A.J.; Looser, U.; Prudhomme, C.; Rees, G.; Stahl, K.; Tallaksen, L.M. Large-scale river flow archives: Importance, current status and future needs. *Hydrol. Process.* **2011**, *25*, 1191–1200.
21. Cloke, H.L.; Pappenberger, F. Ensemble flood forecasting: A review. *J. Hydrol.* **2009**, *375*, 613–626.
22. Smith, L.C. Satellite remote sensing of river inundation area, stage, and discharge. A review. *Hydrol. Process.* **1997**, *11*, 1427–1439.
23. Alsdorf, D.E.; Rodriguez, E.; Lettenmaier, D.P. Measuring surface water from space. *Rev. Geophys.* **2007**, *45*, RG2002.
24. Schumann, G.; Bates, P.D.; Horritt, M.S.; Matgen, P.; Pappenberger, F. Progress in integration of remote sensing-derived flood extend and stage data and hydraulic models. *Rev. Geophys.* **2009**, *47*, RG4001.
25. Kittel, C.M.M.; Jiang, L.; Tottrup, C.; Bauer-Gottwein, P. Sentinel-3 radar altimetry for river monitoring—A catchment-scale evaluation of satellite water surface elevation from Sentinel-3A and Sentinel-3B. *Hydrol. Earth Syst. Sci.* **2021**, *25*, 333–357.

26. Kossieris, S.; Tsiakos, V.; Tsimiklis, G.; Amditis, A. Inland water level monitoring from satellite observations: A scoping review of current advances and future opportunities. *Remote Sens.* **2024**, *16*, 1181.
27. Musa, Z.N.; Popescu, I.; Mynett, A. A review of applications of satellite SAR, optical, altimetry and DEM data for surface water modeling, mapping and parameter estimation. *Hydrol. Earth Syst. Sci.* **2015**, *19*, 3755–3769.
28. Pan, F. Remote sensing of river stage and discharge. *SPIE Newsroom* **2013**. https://doi.org/10.1117/2.1201212.004611.
29. Pan, F.; Nichols, J. Remote sensing of river stage using the cross-sectional inundation area-river stage relationship (IARSR) constructed from digital elevation model data. *Hydrol. Process.* **2013**, *27*, 3596–3606.
30. Pan, F.; Liao, J.; Li, X.; Guo, H. Application of the inundation area-lake level rating curves constructed from the SRTM DEM to retrieving lake levels from satellite measured inundation areas. *Comput. Geosci.* **2013**, *52*, 168–176.
31. Pan, F.; Wang, C.; Xi, X. Constructing River stage-discharge rating curves using remotely sensed river cross-sectional inundation areas and river bathymetry. *J. Hydrol.* **2016**, *540*, 670–687.
32. Pan, F. Accuracy assessment of estimated river water surface elevations from Landsat 8 and 9 imagery among twenty water indices. *Remote Sens.* **2024**, *16*, 3054.
33. Koblinsky, C.J.; Clarke, R.T.; Brenner, A.C.; Frey, H. Measurement of river level variations with satellite altimetry. *Water Resour. Res.* **1993**, *29*, 1839–1848.
34. Brkett, C.M.; Mertes, L.A.K.; Dunne, T.; Costa, M.H.; Jasinski, M.J. Surface water dynamics in the Amazon Basin: Application of satellite radar altimetry. *J. Geophys. Res.-Atmos.* **2002**, *107*, 8059.
35. Coes, M.T.; Brikett, C.M. Calculation of river discharge and prediction of lake height from satellite radar altimetry: Example for the Lake Chad Basin. *Water Resour. Res.* **2004**, *40*, W10205.
36. Kouraev, A.V.; Zakharova, E.A.; Samain, O.; Mognard, N.M.; Cazenave, C. Ob' river discharge from TOPEX/Poseidon satellite altimetry (1992–2002). *Remote Sens. Environ.* **2004**, *93*, 238–245.
37. Calmant, S.; Seyler, F. Continental surface waters from satellite altimetry. *Comptes Rendus Geosci.* **2006**, *338*, 1113–1122.
38. Leon, J.G.; Calmant, S.; Seyler, F.; Bonnet, M.P.; Cauhopé, M.; Frappart, F.; Filizola, N.; Fraizy, P. Rating curves and estimation of average water depth at the upper Negro River based on satellite altimeter data and modeled discharges. *J. Hydrol.* **2006**, *328*, 481–496.
39. Birkinshaw, S.J.; O'Donnell, G.M.; Moore, P.; Kilsby, C.G.; Fowler, H.J.; Berry, P.A.M. Using satellite altimetry data to augment flow estimation techniques on the Mekong River. *Hydrol. Process.* **2010**, *24*, 3811–3825.
40. Bhang, K.L.; Schwartz, F.W.; Park, S. Estimating historic lake stages from one-time snapshot, the Shuttle Radar Topography Mission of 2020. *Hydrol. Process.* **2010**, *34*, 1834–1843.
41. Altenau, E.H.; Pavelsky, T.M.; Moller, D.; Pitcher, L.H.; Bates, P.D.; Durand, M.T.; Smith, L.C. Temporal variations in river water surface elevation and slope captured by AirSWOT. *Remote Sens. Environ.* **2019**, *224*, 304–316.
42. Chipman, J.W. A multisensory approach to satellite monitoring of trends in lake area, water level and volume. *Remote Sens.* **2019**, *11*, 158.
43. Jiang, L.; Anderson, O.B.; Nielsen, K.; Zhang, G.; Bauer-Gottwein, P. Influence of local geoid variation on water surface elevation estimates derived from multi-mission altimetry for Lake Namco. *Remote Sens. Environ.* **2019**, *221*, 65–79.
44. Bandini, F.; Sunding, T.P.; Linde, J.; Smith, O.; Jensen, I.K.; Koppl, C.J.; Butts, M.; Bauer-Gottwein, P. Unmanned aerial system (UAS) observations of water surface elevation in a small stream: Comparison of radar altimetry, Lidar and photogrammetry techniques. *Remote Sens. Environ.* **2020**, *237*, 111487.
45. Tortini, R.; Noujdina, N.; Yeo, S.; Ricko, M.; Birkett, C.; Khandelwal, A.; Kumar, V.; Marlier, M.A.E.; Lettenmaier, D.P. Satellite-based remote sensing data set of global surface water storage change from 1992 to 2018. *Earth Syst. Sci. Data* **2020**, *12*, 1141–1151.
46. Yuan, C.; Gong, P.; Bai, Y. Performance assessment of ICESat-2 laser altimeter data for water level measurement over lakes and reservoirs in China. *Remote Sens.* **2020**, *12*, 770.
47. Frappart, F.; Blarel, F.; Fayad, I.; Berge-Nguyen, M.; Crétaus, J.F.; Shu, S.; Schregenberger, J.; Badhdadi, N. Evaluation of the performances of radar and lidar altimetry mission for water level retrievals in mountainous environment: The case of the Swiss lakes. *Remote Sens.* **2021**, *13*, 2196.
48. Ma, Y.; Xu, N.; Sun, J.; Wang, X.; Yang, F.; Li, S. Estimating water levels and volumes of lakes dated back to the 1980s using Landsat imagery and photo-counting lidar datasets. *Remote Sens. Environ.* **2019**, *212*, 111287.
49. Brakenridge, G.R.; Tracy, B.T.; Knox, J.C. Orbital SAR remote sensing of a river flood wave. *Int. J. Remote Sens.* **1998**, *19*, 1439–1445.
50. Pietroniro, A.; Prowse, T.; Peters, D.L. Hydrologic assessment of an inland freshwater data using multi-temporal satellite remote sensing. *Hydrol. Process.* **1999**, *13*, 2483–2498.

51. Temimi, M.; Leconte, R.; Brissette, F.; Chaouch, N. Flood monitoring over the MacKenzie River Basin using passive microwave data. *Remote Sens. Environ.* **2005**, *98*, 344–355.
52. Matgen, P.; Schumann, G.; Henry, J.P.; Hoffmann, L.; Pfister, L. Integration of SAR-derived river inundation areas, high-precision topographic data and a river flow model toward near real-time flood management. *Int. J. Appl. Earth Obs. Geoinf.* **2007**, *9*, 247–263.
53. Schumann, G.; Pappenberger, F.; Matgen, P. Estimating uncertainty associated with water stages from a single SAR image. *Adv. Water Resour.* **2008**, *31*, 1038–1047.
54. Schumann, G.; Pappenberger, F.; Matgen, P. Conditioning water stages from satellite imagery on uncertain data points. *IEEE Geosci. Remote Sens. Lett.* **2008**, *5*, 810–813.
55. Kebede, M.G.; Wang, L.; Li, X.; Hu, Z. Remote sensing-based river discharge estimation for a small river flowing over the high mountain regions of the Tibetan Plateau. *Int. J. Remote Sens.* **2019**, *41*, 3322–3345.
56. Coss, S.; Durand, M.; Yi, Y.; Jia, Y.; Guo, Q.; Tuozzolo, S.; Shum, C.K.; Allen, G.H.; Calmant, S.; Pavelsky, T. Global River Radar Altimetry Time Series (GRRATS): New river elevation earth science data records for the hydrologic community. *Earth Syst. Sci. Data* **2020**, *12*, 137–150.
57. Fu, L.-L.; Pavelsky, T.; Cretaux, J.-F.; Morrow, R.; Farrar, J.T.; Vaze, P.; Sengenes, P.; Vinogradova-Shiffer, N.; Sylvestre-Baron, A.; Picot, N.; et al. The surface water and ocean topography mission: A breakthrough in radar remote sensing of the ocean and land surface water. *Geophys. Res. Lett.* **2024**, *51*, e2023GL107652. https://doi.org/10.1029/2023GL107652.
58. Guo, Z.; Wu, L.; Huang, Y.; Guo, Z.; Zhao, J.; Li, N. Water-body segmentation for SAR images: Past, Current, and Future. *Remote Sens.* **2022**, *14*, 1752.
59. Mason, D.C.; Schumann, G.J.-P.; Neal, J.C.; Garcia-Pintado, J.; Bates, P.D. Automatic near real-time selection of flood water levels from high resolution Synthetic Aperture Radar images for assimilation into hydraulic models: A case study. *Remote Sens. Environ.* **2012**, *124*, 705–716.
60. Pan, F.; Xi, X.; Wang, X. A comparative study of water indices and image classification algorithms for mapping inland surface water bodies using Landsat imagery. *Remote Sens.* **2020**, *12*, 1611.
61. McFeeters, S.K. The use of the normalized difference water index (NDWI) in the delineation of open water features. *Int. J. Remote Sens.* **1996**, *17*, 1425–1432.
62. Xu, H. Modification of normalized difference water index (NDWI) to enhance open water features om remotely sensed imagery. *Int. J. Remote Sens.* **2006**, *27*, 3025–3033.
63. Feyisa, G.L.; Meilby, H.; Fensholt, R.; Proud, S.R. Automated water extraction index: A new technique for surface water mapping using Landsat imagery. *Remote Sens. Environ.* **2014**, *140*, 23–35.
64. Otsu, N. A threshold selection method from gray-level histograms. *IEEE Trans. Syst. Man Cybern.* **1979**, *9*, 62–69.
65. Market, K.N.; Market, A.M.; Mayer, T.; Nauman, C.; Haag, A.; Poortinga, A.; Bhandari, B.; Thawl, N.S.; Kunlamai, T.; Chishtie, F.; et al. Comparing Sentinel-1 surface water mapping algorithms and radiometric terrain correction processing in Southeast Asia utilizing Google Earth Engine. *Remote Sens.* **2020**, *12*, 2469.
66. Kavats, O.; Khramov, D.; Sergieieva, K. Surface water mapping from SAR images using optimal threshold selection method and reference water mask. *Water* **2022**, *14*, 4030.
67. Chagas, M.C.; Falcão, A.P.; de Oliveira, R.P. Using Sentinel imagery for mapping and monitoring small surface water bodies. *Remote Sens.* **2025**, *17*, 2128.
68. Stone, J.; Rogala, J.; Sattler, S.R.; Hanson, J.L.; Rohweder, J. *Upper Mississippi River System Topobathy*; Data Release; U.S. Geological Survey: Reston, VA, USA, 2016. https://doi.org/10.5066/F7057CZ3.
69. Stone, J.; Hanson, J.L.; Sattler, S.R. *The Upper Mississippi River System—Topobathy*; Fact Sheet 2016-3097; U.S. Geological Survey: Reston, VA, USA, 2017; p. 4. https://doi.org/10.3133/fs20163097.
70. Rogala, J.T. Methodologies Employed for Bathymetric Mapping and Sediment Characterization as Part of the Upper Mississippi River System Navigation Feasibility Study. In *ENV Report 13, Interim Report for the Upper Mississippi River–Illinois Waterway System Navigation Study*; U.S. Army Engineer Districts, Rock Island, St. Louis, and St. Paul; U.S. Army Corps of Engineers: Washington, D.C., USA, 1999.
71. Sauer, V.B.; Turnipseed, D.P. Stage Measurement at Gaging Stations. In *U.S. Geological Survey Techniques and Methods.*; Book 3; U.S. Geological Survey: Reston, VA, USA, 2010; Volume A7, p. 45. https://doi.org/10.3133/tm3A7.
72. European Space Agency (ESA) Sentinel Application Platform (SNAP). Available online: https://earth.esa.int/eogateway/tools/snap (accessed on 29 October 2026).
73. Filipponi, F. Sentinel-1 GRD Preprocessing Workflow. *Proceedings* **2019**, *18*, 11. https://doi.org/10.3390/ECRS-3-06201.

74. Richards, J.A. *Remote Sensing Digital Image Analysis: An Introduction*, 5th ed.; Springer: Berlin/Heidelberg, Germany, 2013; p. 494.
75. Chow, V.T. *Open-Channel Hydraulics*; McGraw-Hill Book Company: New York, NY, USA, 1959; p. 680.
76. Henderson, F.M. *Open Channel Flow*; MacMillan: New York, NY, USA, 1966; p. 522.
77. Pan, F.; Smith, R.B. Gap winds and wakes: SAR observations and numerical simulations. *J. Atmos. Sci.* **1999**, *56*, 905–923.
78. World Meteorological Organization. Guide to meteorological instruments and methods of observation. In *WMO-No.8*, 8th ed.; World Meteorological Organization: Geneva, Switzerland, 2018; p. 1166.

Disclaimer/Publisher's Note: The statements, opinions and data contained in all publications are solely those of the individual author(s) and contributor(s) and not of MDPI and/or the editor(s). MDPI and/or the editor(s) disclaim responsibility for any injury to people or property resulting from any ideas, methods, instructions or products referred to in the content.